

See discussions, stats, and author profiles for this publication at: <https://www.researchgate.net/publication/244478898>

Gold(III) Complexes of Pyridyl- and Isoquinolylamido Ligands: Structural, Spectroscopic, and Biological Studies of a New Class of Dual Topoisomerase I and II Inhibitors

ARTICLE *in* INORGANIC CHEMISTRY · JULY 2013

Impact Factor: 4.76 · DOI: 10.1021/ic400339z · Source: PubMed

CITATIONS

6

READS

28

5 AUTHORS, INCLUDING:



[Wanvipa Ruangpradit](#)

Topogen Inc

2 PUBLICATIONS 11 CITATIONS

[SEE PROFILE](#)



[Mark T. Muller](#)

University of Central Florida

141 PUBLICATIONS 3,427 CITATIONS

[SEE PROFILE](#)



[Orde Q Munro](#)

University of the Witwatersrand

87 PUBLICATIONS 1,278 CITATIONS

[SEE PROFILE](#)

Gold(III) Complexes of Pyridyl- and Isoquinolylamido Ligands: Structural, Spectroscopic, and Biological Studies of a New Class of Dual Topoisomerase I and II Inhibitors

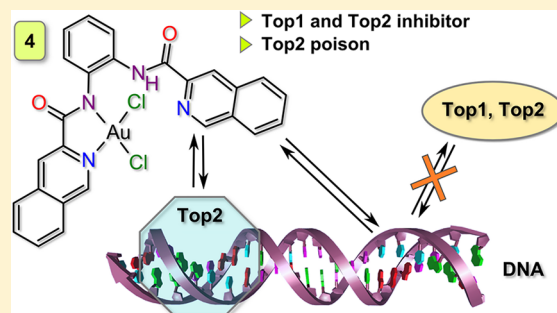
Colin R. Wilson,[†] Alexander M. Fagenson,[‡] Wanvipa Ruangpradit,[‡] Mark T. Muller,[‡] and Orde Q. Munro^{*,†}

[†]School of Chemistry and Physics, University of KwaZulu-Natal, Private Bag X01, Scottsville 32009, South Africa

[‡]College of Medicine, University of Central Florida, Biomolecular Research Annex, 12722 Research Parkway, Orlando, Florida 32826-3227, United States

Supporting Information

ABSTRACT: The structures, spectroscopy, and cytotoxicity of four novel nominally square-planar gold(III) chelates **1–4** with the general formula *cis*-AuCl₂(X), where the ligand X is an anionic bidentate pyridyl- or isoquinolylamido chelating agent, are described. The Au–N_{amido}, Au–N_{pyridyl}, and Au–N_{isoquinolyl} distances are 2.002(9)–2.016(3), 2.01(1)–2.037(3), and 2.037(3) Å, respectively. Density functional theory simulations afforded accurate gold(III) coordination geometries for **1–4** (bond distances and angles to within 5% of the X-ray values), while accurate transition energies were limited to those calculated in the UV spectral region. The complexes had variable stability in dimethyl sulfoxide: compound **3** (relatively rigid) was indefinitely stable, compounds **1** and **2** (conformationally flexible) slowly demetalated over 30 days, and **4** (extensively aromatic) formed an insoluble precipitate after 10 days (72 h in an aqueous buffer). The isoquinolylamido derivative **4** was sufficiently cytotoxic in the NCI-60 screen to undergo full five-dose testing. Notably low GI₅₀ (1.8, 2.3, and 3.2 μM) and IC₅₀ (4.0, 9.8, and 15 μM) values were recorded for the OVCAR-3, IGROV1, and SW-620 cell lines, respectively. Hierarchical cluster analysis employing the National Cancer Institute (NCI) data for known anticancer drugs and **4** revealed that compound **4** is mechanistically identical with the topoisomerase IIα (Top2) poison zorubicin and statistically similar to the topoisomerase IB (Top1) poisons camptothecin and 9-methoxycamptothecin. The Top2-catalyzed decatenation reaction of kinetoplast DNA was studied as a function of the concentration of **4**: the compound acts as an interfacial poison of Top2 at low concentrations (<1 μM) and a catalytic inhibitor of the enzyme above 5 μM. Gel mobility shift assays (plasmid DNA substrate) showed that the catalytic inhibition of Top2 likely correlates with DNA binding by **4** at concentrations >5 μM. Compound **4** is also a catalytic inhibitor of Top1 at higher concentrations, consistent with DNA binding by the complex.



INTRODUCTION

The first report (1965)¹ that DNA-targeting^{2,3} cisplatin inhibited mitosis in bacteria and the subsequent clinical deployment of cisplatin and its analogues^{4,5} as anticancer metallodrugs^{6,7} have fueled the growth of multidisciplinary studies on square-planar platinum(II) complexes⁸ for several decades.^{9–11} More recently, isoelectronic (d⁸) square-planar gold(III) complexes have been featured in metallodrug development efforts as the quest for drug diversity and novel compounds to overcome cisplatin-resistant tumor cell lines has escalated.^{12–17} Despite the expectation that gold(III) complexes might act in a fashion similar to that of platinum(II) complexes in biological systems, gold(III) complexes differ significantly and are especially susceptible to reduction to Au^I and colloidal gold, Au⁰.¹⁸ Ligand design is thus crucial to stabilizing the Au^{III} oxidation state for use in normal solutions and physiological media.^{19,20}

Chemical strategies for imparting redox stability to gold(III) complexes typically involve the use of chelating and macrocyclic ligands containing strong neutral or anionic σ-donor atoms (C, N, and O to match the hard Au^{III} ion). Tetradentate macrocyclic ligands block ligand-exchange reactions at the metal center, e.g., the binding of S-donor reducing ligands, while powerful σ-donor chelating ligands transfer electron density to the metal center and thus lower the reduction potential of the Au^{III} ion.²¹ Examples of Au^{III}-stabilizing chelating ligands are porphyrins [e.g., TPP (*meso*-tetraphenylporphyrin dianion)],^{22,23} terpy (2,2';6',2"-terpyridine),^{24,25} glycyldistimidate,²⁶ dithiocarbamates,²⁷ cyclam (1,4,8,11-tetraazacyclotetradecane),^{21,28} and damp (2-[((dimethylamino)methyl]phenyl)].^{29–31} Not all gold(III) complexes involving

Received: February 8, 2013

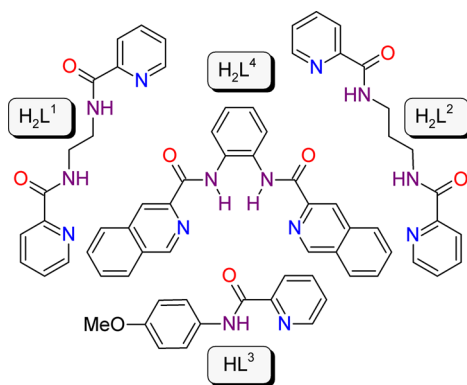
Published: July 1, 2013

these chelating ligands are uniformly active against cancer. At present, only a handful show significant cytotoxicity: $[\text{Au}^{\text{III}}(\text{bipy}-\text{H})(\text{OH})][\text{PF}_6]$ [bipy-H, deprotonated 6-(1,1-dimethylbenzyl)-2,2'-bipyridine],³² $\text{Au}^{\text{III}}(\text{dmamp})\text{Cl}_2$ [dmamp, 2-(dimethylaminomethyl)phenyl],^{29,33} $[\text{Au}^{\text{III}}(\text{DMDT})\text{X}_2]$ and $[\text{Au}^{\text{III}}(\text{ESDT})\text{X}_2]$ (DMDT, *N,N*-dimethylidithiocarbamate; ESDT, ethylsarcosinedithiocarbamate; X = Cl or Br),²⁷ $[\text{Au}^{\text{III}}(\text{Porph})]^+$ (Porph, porphyrin dianion)^{34–39} and $[\text{Au}^{\text{III}}_m(\text{C}^{\text{N}}\text{N}^{\text{C}})_m\text{L}]^{n+}$ ($m = 1–3$; C^NN^C, diphenylpyridine).⁴⁰ The biological targets, furthermore, are quite varied and include DNA/topoisomerase I (Top1) for the cyclometalated C^NN^C gold(III) adduct^{40,41} and gold(III) porphyrins,²³ protein targets such as Bcl-2 and histone deacetylase (HDAC) for gold(III) porphyrins,⁴² and proteasome inhibition for gold(III) dithiocarbamates.^{19,43}

Relatively few amidogold(III) complexes have been synthesized and characterized or evaluated for their potential cytotoxicity. In one of the earliest structure-focused studies of these compounds, Cheung et al. reported the complex $\text{Au}^{\text{III}}(\text{HL})\text{Cl}_2$ [H_2L , 2,2'-bis(2-pyridylcarboxamide)-1,1'-binaphthalyl].⁴⁴ Rather unexpectedly, the Au^{III} ion was chelated to half of the tetradentate ligand via amido and pyridyl N-donor atoms, leaving a pair of *cis*-Cl[–] ions to complete the square-planar coordination geometry and an unbound amide moiety.⁴⁴ This coordination mode, while not anticipated from the ligand's structure, presumably reflects bridge-impeded chelation of the metal by all donor atoms or other factors related to substitution of the Cl[–] ions. The modest cytotoxicity profiles and limited solution stability under physiological conditions of a series of tetradentate bis(amido)gold(III) chelates have recently been reviewed alongside data for gold(III) porphyrins and Au^{III}-salen derivatives.⁴⁵ Of relevance to the present work, Yang and co-workers reported that, out of a small series of three tridentate amidogold(III) complexes, at least one compound, $[\text{Au}(\text{Quinpy})\text{Cl}]\text{Cl}$ [Quinpy, *N*-(8-quinoly)pyridine-2-carboxamido], had reasonable solution stability, was capable of binding calf-thymus DNA, and had quite promising cytotoxicity against melanoma and lung cancer cell lines.⁴⁶ These authors also showed that a mono(amido)gold(III) complex, $[\text{Au}(\text{L-N,N'})\text{Cl}_2]$ [L-N,N', *N*-(4-methylphenyl)-2-pyridinecarboxamide], reacted with 2 equiv of 5'-guanosine monophosphate (5'-GMP) via substitution of the Cl[–] ions to give the bis(5'-GMP) adduct.⁴⁷

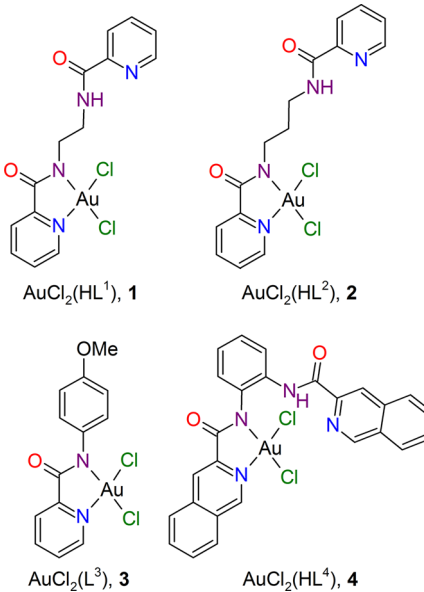
In this paper, we describe the synthesis and characterization of novel H_2L^4 (Scheme 1) and the mono(amido)gold(III) chelates formed by the deprotonated ligand L³ and hemi-

Scheme 1. Free Ligand Structures



deprotonated ligands HL¹, HL², and HL⁴ (Scheme 2). Single-crystal X-ray structures were determined for H_2L^4 and the

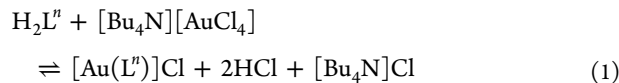
Scheme 2. Structures of the Gold(III) Pyridyl- and Isoquinolylamido Chelates Studied in This Work



gold(III) complexes 1–4. The ligands H_2L^1 , H_2L^2 , and HL^3 have been described previously in the literature.^{48–51} Density functional theory (DFT) simulations have been used to delineate the electronic structures of 1–4. The cytotoxicity profiles of compounds 2–4 were evaluated by the National Cancer Institute (NCI) using their panel of 60 human cancer cell lines. The cytotoxicity of compound 4 warranted further investigation of its DNA affinity and ability to target human topoisomerase I and II (Top1 and Top2).

RESULTS AND DISCUSSION

From inception, a key objective of this work was to synthesize structurally unique, predominantly planar cationic tetradentate bis(amido)gold(III) complexes that could potentially act as cytotoxic DNA intercalators—a goal inspired in part by the biochemistry and molecular biology of cationic gold(III) porphyrins.²² The reaction of H_2L^n ($n = 1, 2, 4$) with Au^{III} was expected to give potentially cytotoxic cationic tetradentate $\text{AuN}_2\text{N}'_2$ trischelates of the metal (eq 1).



However, despite several attempts to synthesize the target salts $[\text{Au}(\text{L}^n)]\text{Cl}$ (Scheme S1, Supporting Information), and in consonance with the earlier literature on similar pyridylamido complexes of gold(III),⁴⁴ only the neutral *cis*-dichlorogold(III) complexes 1–4 could be isolated. Evidently, the Au–Cl bonds in this system are substitution-inert [in contrast to the analogous palladium(II) complexes⁵²]. Notwithstanding the intractable synthesis of the target $\text{AuN}_2\text{N}'_2$ trischelates, the new complexes 1–4 were deemed worthy of comprehensive structural, spectroscopic, and cytotoxicity studies.

Molecular Structure of H_2L^4 . The X-ray crystal structure of the novel ligand H_2L^4 is shown and briefly discussed in the Supporting Information (Figures S1 and S2) because the

primary focus of this work is on the chemistry and molecular biology of **1–4**. However, one notable feature of the structure of H_2L^4 is its markedly nonplanar conformation brought about by an intramolecular hydrogen bond involving the N–H donor of one amide group and the carbonyl O of the other. The ligand is therefore not preorganized for tetradentate chelation of a square-planar metal ion.

Molecular Structures of 1–3. The X-ray structures of **1–3** are shown in Figure 1. The Au^{III} ion is nominally square

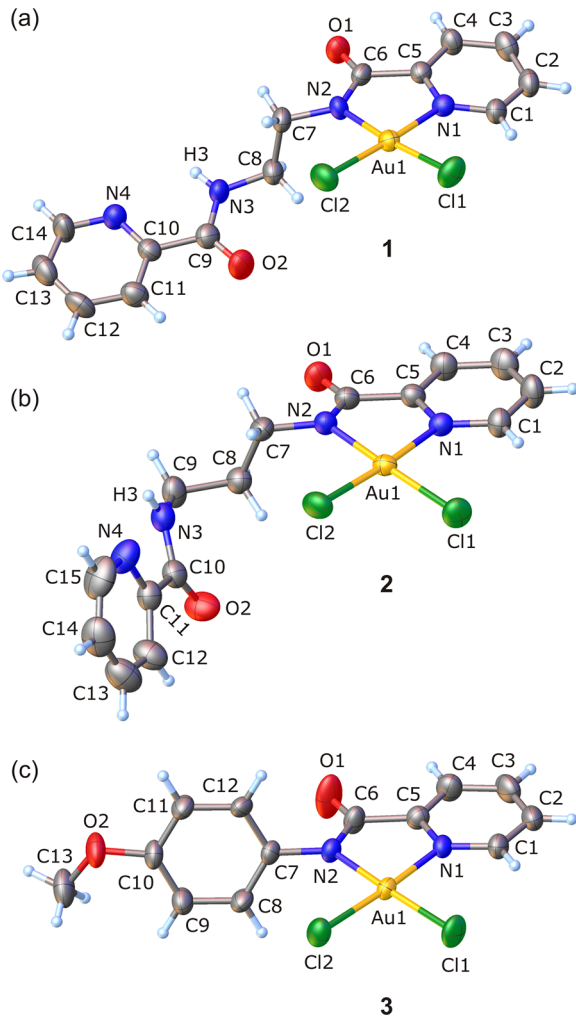


Figure 1. Labeled views of single-crystal X-ray structures of gold(III) chelates **1** (a), **2** (b), and **3** (c). H atoms are rendered as spheres of uniform arbitrary radii, and bonds are represented as cylinders. Thermal ellipsoids are represented as 50% probability surfaces for **1** and **3** and 40% probability surfaces for **2**.

planar in each complex with a pair of *cis*- Cl^- ions coordinated trans to the single pyridylamido chelating moiety of the ligand in the case of **3** and one of the pair of such chelating groups in **1** and **2**. The substituent groups attached to the deprotonated metal-bound amide N atom (N2) in **1–3** adopt structure-dependent conformations that have an essentially minimal impact on the coordination geometry of the Au^{III} ion in each case (Table 1). The aryl-substituted derivative **3** has coordination group parameters that are structurally and statistically equivalent to the alkyl-substituted analogues **1** and **2**, despite having a substituent that may conjugate with the amide-based chelate ring.

The $\text{Au}-\text{N}_{\text{pyridine}}$ and $\text{Au}-\text{N}_{\text{amido}}$ distances for the pyridine-based chelates **1–3** average 2.035(3) and 2.014(5) Å, respectively; these values indicate crystallographically and chemically distinct coordination interactions. Both N-donor atom types (pyridine and amido) are sp^2 -hybridized; however, as might be anticipated for an anionic N-donor atom (and, consequently, a more powerful σ donor), the $\text{Au}-\text{N}$ distance to the amido N is more than 3 standard deviations shorter than that to the pyridine N. This phenomenon has been observed in the crystal structures of other amidogold(III) chelates.^{53,54} Regarding the dissimilar $\text{Au}-\text{N}$ bonds in pyridylamido chelates, it is noteworthy that symmetric bipyridine (bipy) complexes of gold(III) such as $[\text{AuCl}_2(\text{DMbipy})][\text{PF}_6]$ and $[\text{AuCl}_2(\text{DMObipy})][\text{PF}_6]$, where DMbipy = 4,4'-dimethyl-2,2'-bipyridine and DMObipy = 4,4'-dimethoxy-2,2'-bipyridine, exhibit equivalent $\text{Au}-\text{N}_{\text{pyridine}}$ distances of 2.03(1) and 2.02(2) Å, respectively.⁵⁵ This confirms the notion that the amido and pyridine N atoms are chemically distinct (despite equivalent hybridization), with the former acting as a strong σ donor and the latter as a more balanced π donor/ π acceptor,^{56,57} and that this electronic distinction underpins dissymmetric coordination of the Au^{III} ion in the present compounds.

The $\text{Au}-\text{Cl}1$ (trans to the amido group) and $\text{Au}-\text{Cl}2$ (trans to the pyridine group) bond distances for **1–3** average 2.291(4) and 2.270(13) Å, respectively. Closer inspection of the $\text{Au}-\text{Cl}$ distances indicates that a significant “trans effect”^{58,59} is structurally manifest in these complexes, as briefly noted in an earlier paper by Fan et al.⁵⁴ More specifically, the $\text{Au}-\text{Cl}$ bond trans to the stronger σ -donor atom (N2, or N_{amido}) is considerably longer than that trans to the pyridine N; in the case of **3**, this difference is as large as 0.034 Å and thus statistically significant relative to the standard uncertainties of the experimental $\text{Au}-\text{Cl}$ bond distances. The difference between the coordination of chloride trans to the amido group relative to the pyridine group in **1–3** becomes particularly apparent if we compare the mean $\text{Au}-\text{Cl}1$ distance above to the mean $\text{Au}-\text{Cl}$ distance of 2.255(7) Å reported for the symmetric bipy derivatives $[\text{AuCl}_2(\text{DMbipy})][\text{PF}_6]$ and $[\text{AuCl}_2(\text{DMObipy})\text{Cl}_2][\text{PF}_6]$.⁵⁵ These complexes typify the expected metrics for the coordination of chloride trans to an $\text{Au}-\text{N}_{\text{pyridine}}$ bond in a symmetric five-membered chelate ring system and highlight the marked elongation of the $\text{Au}-\text{Cl}$ bonds trans to the amido N donor in the present complexes (especially **3**). Interestingly, if the chelating σ -donor anion coordinated to Au^{III} is switched to C, as in the complex $\text{AuCl}_2(2\text{-phenylpyridine})$,⁶⁰ then a very large structural trans effect occurs, with the $\text{Au}-\text{Cl}$ distance trans to the $\text{Au}-\text{C}$ bond elongating beyond that observed here to 2.361(8) Å. As might be anticipated, the structural trans effect discussed above for organometallic gold complexes is paralleled by a kinetic trans effect in the substitution reactions of the Au^{III} ion. Anions such as chloride coordinated trans to a powerful σ donor (e.g., C_6H_5^-) are kinetically more labile than those coordinated cis to the “labilizing” ligand.⁶¹ This reactivity pattern clearly correlates with a longer, weaker $\text{Au}-\text{Cl}$ bond trans to the strong σ -donor ligand in the structures of such compounds. One might logically expect that, for **1–3**, substitution of at least one of the chloride ions (with that trans to the amido group presumably being more reactive) might occur with some nucleophiles.

The bond angles subtended at the metal ion in **1–3** (Table 1) are normal for five-membered ring chelates of Au^{III} with two N-donor atoms. The mean *cis* $\text{Cl}-\text{Au}-\text{Cl}$ bond angle is 89.1(2)°; the mean *cis* $\text{N}-\text{Au}-\text{N}$ angle is more acute,

Table 1. Selected Crystallographic and DFT-Calculated Bond Distances and Bond Angles for 1–4

	1		2		3		4	
	X-ray	DFT	X-ray	DFT	X-ray	DFT	X-ray	DFT
Bond Distances								
Au1–N1	2.036(5)	2.07	2.037(3)	2.07	2.031(4)	2.08	2.048(3)	2.07
Au1–N2	2.019(4)	2.04	2.014(3)	2.04	2.009(5)	2.06	2.035(3)	2.07
Au1–Cl1	2.290(2)	2.34	2.287(1)	2.34	2.295(2)	2.35	2.303(1)	2.36
Au1–Cl2	2.285(2)	2.3	2.263(1)	2.3	2.261(2)	2.31	2.270(1)	2.31
C=O ^a	1.211(7)	1.22	1.230(5)	1.22	1.21(1)	1.22	1.232(4)	1.21
C=O ^b	1.228(7)	1.22	1.217(5)	1.22			1.240(6)	1.22
N–C ^a	1.345(8)	1.35	1.341(5)	1.35	1.343(9)	1.36	1.362(5)	1.37
N–C ^b	1.340(7)	1.35	1.346(6)	1.35			1.391(5)	1.36
Bond Angles								
N1–Au1–Cl1	94.0(1)	94.5	94.85(9)	94.5	95.3(1)	94.5	95.68(8)	94.3
Cl1–Au1–Cl2	89.11(7)	89.6	89.00(4)	89.3	88.87(6)	89.7	89.42(2)	90.2
Cl2–Au1–N2	95.8(1)	95.3	94.90(9)	95.6	94.4(1)	95.4	93.83(9)	94.8
N2–Au1–N1	81.0(2)	80.6	81.3(1)	80.6	81.5(2)	80.5	81.1(1)	80.7
Au1–N1–C5 ^c	112.9(4)	113	112.9(3)	113	113.2(4)	113	112.7(2)	113
Au1–N2–C6 ^d	115.3(4)	116	115.0(3)	116	115.2(4)	115	116.0(2)	115
N1–C5–C6 ^e	115.9(5)	117	115.9(4)	117	116.2(5)	118	116.7(3)	118
N2–C6–C5 ^f	113.6(5)	114	113.7(3)	114	113.9(6)	114	113.0(3)	114

^aMetal-bound amide group. ^bFree amide group. ^cFor 4, this angle is Au1–N1–C9. ^dFor 4, this angle is Au1–N2–C9. ^eFor 4, this angle is N1–C9–C10. ^fFor 4, this angle is N2–C10–C9.

measuring 81.2(2)°. The latter bond angle, which deviates significantly from 90°, clearly reflects the geometric constraints on metal-ion coordination imposed by the five-membered chelate ring and compares favorably with equivalent values in the literature, which range from 80.6(2)° for [AuCl₂(bipy)]-[NO₃]⁶² to 81.42(7)° for AuCl₂(N-NP2C), where N-NP2C = N-nonylpyridine-2-carboxamido anion.⁵³ (Amidopyridine- and bipy-type ligands have similar “bite” angles.) In each complex, the cis N–Au–Cl bond angles are equivalent, averaging 95.0(7)° and 94.7(8)° for the angles to Cl1 and Cl2 for 1–3, respectively.

Gold chelates 1–3 are polyfunctional in the sense that they possess hydrogen-bond donor and acceptor groups as well as aromatic ring systems. The supramolecular structures of the compounds are accordingly both diverse and quite complex. Largely because of the lack of cytotoxicity of 1–3 relative to 4 (as discussed later), brief comments on hydrogen-bonding and π-stacking interactions in their crystal structures are given in the Supporting Information (Figures S3–S12).

Crystal and Molecular Structure of 4. The X-ray structure of 4 (Figure 2) is similar in its overall nominally square-planar coordination geometry to the preceding compounds and alike in conformation to 3 insofar as the dihedral angle between the aryl ring (C11–C16) appended to the metal-bound amido group (N2) and the 13-atom mean plane of the isoquinolylamidogold(III) chelate (Au1, N1, C1–C10, and N2) is near-orthogonal, measuring 80.7°. From Table 1, the Au–N_{amide} and Au–N_{IQ}, where IQ = isoquinoline, bond distances of 4 follow the same pattern as the Au–N distances of 1–3, namely, that the bond to the amido group [Au1–N2, 2.035(3) Å] is 4 standard deviations (4σ) shorter than the bond to the isoquinoline N [Au1–N1, 2.048(3) Å]. This, as with 1–3, reflects the fact that the amido group N atom is a more powerful σ donor (Lewis base) than the “pyridine” N atom of the isoquinoline group and distinctly parallels the pK_a’s of the two different donor types: pK_a(N_{amide}) > 10;⁶³ pK_a(N_{IQ}) ~ 5.5.⁶⁴ The cis Au–Cl bonds of 4 exhibit the same asymmetry observed in 1–3, namely, that the Au–Cl bond trans to the

amido N donor is significantly longer (by 0.033 Å) than that trans to the isoquinoline N atom. The magnitude of this structural difference is equivalent, within 1σ, to that observed for 3 and reflects a sizable trans effect induced by the amido group (vide supra). The absolute value of the Au1–Cl1 bond in 4 [2.303(1) Å] is ca. 5% longer than the mean distance for this bond in 1–3 [2.291(3) Å], a relatively insignificant difference, while the Au1–Cl2 bond distance trans to the isoquinoline N atom exactly matches the average distance for this bond type in chelates 1–3 [2.270(11) Å].

The coordination geometry of the Au^{III} ion in compound 4 is structurally distinct from that seen in 1–3 in a substantial aspect. Specifically, the isoquinoline-based chelate system of 4 favors significantly longer Au–N bonds. Thus, the Au–N_{amide} bond of 4 measures 2.035(3) Å and is more than 4 standard deviations (4σ) longer than the mean Au–N_{amide} bond of 1–3 [2.014(5) Å]; similarly, the Au–N_{IQ} bond of 4 [2.048(3) Å] is more than 4σ longer than the mean Au–N_{pyridine} bond distance for 1–3 [2.035(3) Å]. Note that this structural difference exists despite the pK_a of pyridine (5.2) being roughly the same as that for isoquinoline (5.5).⁶⁴ Elongation of the Au–N bonds in 4 reflects coordination of the Au^{III} ion by a poorer σ-donor and/or π-acceptor ligand, with all other structural parameters being equivalent. Inspection of the chelate ring angles for 1–4 (Table 1) confirms that pyridyl- and isoquinolylamido chelate ring systems are indeed metrically equivalent (the N2–Au1–N1, Au1–N1–C5, Au1–N2–C6, N1–C5–C6, and N2–C6–C5 bond angles differ by <1° across the series for each chemically unique bond angle). Note that isoquinoline itself is a slightly stronger-field ligand than pyridine because of its marginally higher pK_a or Lewis basicity, and better π-acceptor ability in square-planar complexes of nickel(II).⁶⁵ The underlying reasons for elongation of the Au–N bond distances in 4 are therefore likely to be electronic, as opposed to structural, in origin but are clearly more complicated than a simplistic interpretation based on extrapolation of the electronic properties of isoquinoline complexes of nickel(II) to the present system. Notably, the DFT-calculated Au–N_{amide} bond

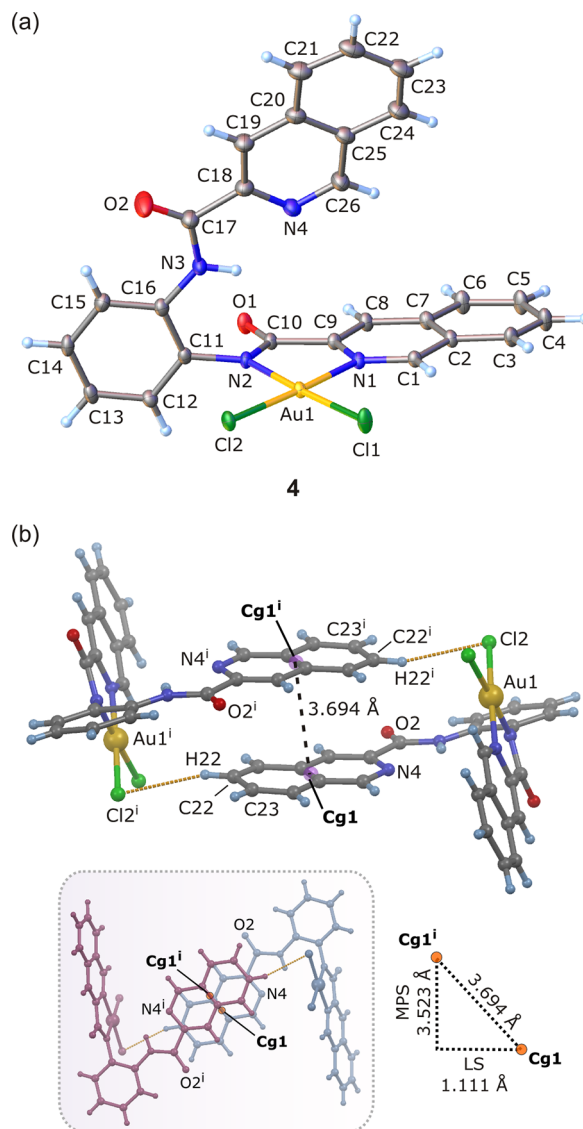


Figure 2. (a) Labeled thermal ellipsoid view (50% probability surfaces) of the low-temperature X-ray structure of **4**. Bonds are rendered as cylinders and H atoms as spheres of uniform arbitrary radii. The solvent (diethyl ether) has been omitted for clarity. (b) Partially labeled view of the centrosymmetric π -stacked dimer formed by **4**. The isoquinoline ring planes are parallel; the distance between the isoquinoline ring centers of gravity ($Cg_1 \cdots Cg_1^i$) is indicated. The mean-plane separation (MPS) and lateral shift (LS) of the stacked isoquinoline rings (calculated from the coordinates of Cg_1 and Cg_1^i) are depicted graphically on the triangle to the right of the top-down view of the dimer (lower left). The dimer is additionally stabilized by C–H \cdots Cl hydrogen bonds: $H_{22} \cdots Cl_2^i$, 2.960(1) Å; $C_{22} \cdots Cl_2^i$, 3.864(4) Å; $C_{22} \cdots H_{22} \cdots Cl_2^i$, 159.5(3)°. Crystallographic symmetry code: (i) $-x, 1 - y, 1 - z$.

distances parallel the experimental trend, consistent with a fundamental difference between the pyridyl- and isoquinolylamido chelate ring systems.

The supramolecular structure of **4** is dominated by unconventional C–H \cdots O and C–H \cdots Cl hydrogen bonds (Figure S12 in the Supporting Information), as with **1–3**. These interactions allow **4** to form one-dimensional hydrogen-bonded chains parallel to the *c* axis of the unit cell. More interesting, however, is the structure of the centrosymmetric hydrogen-bond-stabilized π -stacked dimer formed by **4** (Figure

2b). The metal-free isoquinoline rings of two neighboring molecules of **4** stack with exactly parallel ring planes about a center of inversion to form a relatively tight interaction with a mean-plane separation of 3.523 Å that is well within the 3.35–3.8 Å range expected for π -stacked aryl rings.⁶⁶ If the isoquinoline atom N4 is used as a frame of reference, then the geometry of the interacting isoquinoline rings is the typical offset antiparallel arrangement (N4 atoms pointing in opposite directions) for aromatic N-heterocycles.⁶⁷ This particular ring \cdots ring arrangement evidently represents energetically favorable dipole alignments in the two-ring systems. The distance between the centers of gravity of the two isoquinoline rings, $Cg_1 \cdots Cg_1^i$, measures 3.694 Å such that the lateral shift of the ring systems is 1.111 Å. As is lucidly presented and discussed by Janiak,⁶⁷ the laterally displaced ring systems seen in **4** would permit optimal π \cdots σ attraction between stacked isoquinoline groups in addition to normal London forces of attraction. Isoquinoline and quinoline ring systems are, of course, well-known for their π -stacking ability and are often key pharmacophores prevalent in many anticancer,^{68–70} antiviral,⁷¹ and antitrypanosome⁷² compounds with a mechanism of action (MOA) involving DNA binding by intercalation.⁷³ Of special relevance to the present work, we note that the clinically deployed anticancer drug camptothecin (CPT; a quinoline alkaloid) poisons human Top1 by DNA intercalation at a 5'-TA-3' dinucleotide site targeted for covalent binding by the enzyme during its catalytic cycle.⁷⁴ A final point on the structure of the π -stacked dimer of **4** is that, in addition to π \cdots π interactions between the isoquinoline rings, a symmetry-related pair of unconventional C–H \cdots Cl hydrogen bonds between an isoquinoline ring hydrogen donor (H22) and the coordinated chloride ion acceptor of the neighboring molecule (Cl2ⁱ) stabilizes the interaction. In short, the auxiliary (metal-free) isoquinoline ring of **4** is clearly a potentially useful functional group that may engage in interactions with biological targets such as DNA by π stacking as well as hydrogen bonding.

IR and NMR Spectroscopy. For the three bis(amide) ligands H_2L^1 , H_2L^2 , and H_2L^4 and their corresponding mono(chelate) gold(III) complexes **1**, **2**, and **4**, the single amide carbonyl band, $\nu(CO)$, observed in the IR spectrum of the free ligand splits into two separate signals after chelation of gold(III) by one of the pair of amide groups. From Table 2, the C=O stretching mode of the metal-free amide group, $\nu_2(CO)$, occurs at a higher frequency than that for the metal-bound amide group, $\nu_1(CO)$. The frequency drop for the metal-bound amide group is largest for **2** ($\Delta\nu_{2,1} = 22\text{ cm}^{-1}$) and smallest for

Table 2. Experimental and DFT-Calculated IR Data (Amide Carbonyl Group Region) for **1–4^{a,b}**

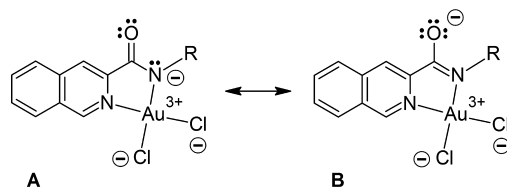
	$\nu_1(CO)/\text{cm}^{-1}$			$\nu_2(CO)/\text{cm}^{-1}$			$\Delta\nu_{2,1}/\text{cm}^{-1}$	
	expt	DFT	diff	expt	DFT	diff	expt	DFT
1	1647	1757	110	1667	1795	128	20	38
2	1645	1757	112	1667	1789	122	22	32
3	1643	1767	124	na	na	na	na	na
4	1652	1772	120	1668	1791	123	16	19

^aAbbreviations: $\nu_1(CO)$ and $\nu_2(CO)$ are the stretching frequencies for the metal-bound and free amide carbonyl groups, respectively; $\Delta\nu_{2,1}$ is the difference between ν_2 and ν_1 , i.e., $\nu_2 - \nu_1$; expt, experimental frequency; diff, difference between the DFT-calculated and experimental frequencies; na, not applicable. ^bExperimental wavenumbers are accurate to $\pm 1\text{ cm}^{-1}$.

4 ($\Delta\nu_{2,1} = 16 \text{ cm}^{-1}$). The DFT-calculated frequencies for the C=O modes of the metal-bound and free amide groups are between 110 and 128 cm^{-1} higher than the experimental frequencies. A mean scaling factor of 0.933 may therefore be used to correct the DFT-simulated spectra for assigning experimental IR bands. This scaling factor, which accounts for phase differences between the solid-state and gas-phase spectra as well as intrinsic shortfalls of the theoretical method, is similar to that widely used for simulations at the B3LYP/6-31G(d) level of theory (0.961).⁷⁵ The DFT-calculated values of $\Delta\nu_{2,1}$ are in reasonably good agreement with the experimental values, with the degree of similitude best for compound **4**. Moreover, the gas-phase DFT-calculated values of $\nu_1(\text{CO})$ decrease linearly with increasing C–O bond distance for **1–4** (Figure S13 in the Supporting Information). This is the expected trend as the C–O bond order decreases. A similar correlation does not exist for the experimental frequencies and bond distances, possibly because of inherent limitations in the accuracy of the ambient-temperature X-ray data for **1–3**.

An explanation for the shift to lower wavenumber for the metal-bound amide band, $\nu_1(\text{CO})$, relative to the free amide band is that the resonance hybrid structure for the chelate lies somewhere between the two resonance forms **A** ($-\text{N}-\text{C}=\text{O}$) and **B** ($\text{N}=\text{C}-\text{O}^-$) illustrated in Scheme 3. Because a decrease

Scheme 3. Illustration of Bond Resonance Involving the Metalbound Amide Group of **4 (by Way of Example)^a**



^aLone pairs of electrons are shown for the amide group to aid visualization of the two resonance forms. The group R represents the chemically distinct remainder of the structure of complex **4** (Scheme 2).

in the C–O bond order is expected to reduce the frequency of the normal mode of vibration for the carbonyl group (Figure S13 in the Supporting Information), the experimental data suggest that the resonance hybrid structures of chelates **1–4** lie slightly closer to resonance form **B** than form **A**, consistent with the behavior previously deduced by Rosenberg for several peptide chelates of copper(II).⁷⁶ Resonance form **B** has a higher N–C bond order, or more N=C double-bond character, than form **A**. The X-ray data for **4** (Table 1) confirm that the N–C bond for the metal-bound amide group [1.362(S) Å] is shorter than that for the metal-free amide group [1.391(S) Å], consistent with a more delocalized electronic structure for the amide group of the chelate ring and, consequently, a slightly higher N–C bond order. One caveat here is that the DFT-calculated C–N bond distances for the metal-bound and free amide groups of **4** are essentially equivalent and do not follow the experimental data. Furthermore, when averaged over functional group type, the X-ray data (Table S2 in the Supporting Information) do not collectively delineate statistically meaningful differences in the mean C–O and N–C bond distances for the metal-bound and free amide groups of **1–4** because of intrinsic resolution limits in the diffraction data. The IR data in the carbonyl frequency region for **1**, **2**, and **4** (i.e., independent CO modes for the

distinct amide groups) are consistent with previous spectral data reported for a comparable mono(amido) chelate of gold(III).⁴⁴

The ^1H NMR spectrum for the free ligand H_2L^4 exhibits an “all-aromatic” proton spectrum with signals spanning the 7–11 ppm range (Figure 3). The chemically and magnetically

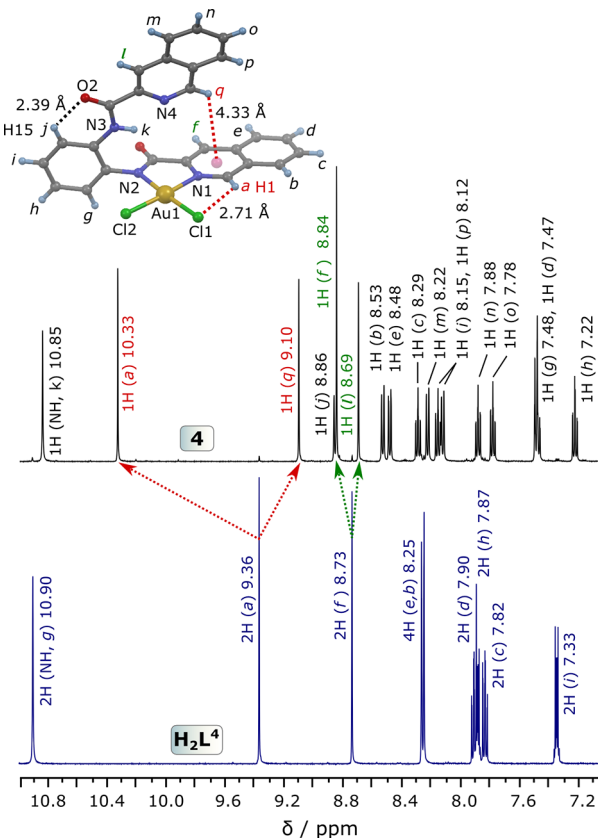


Figure 3. ^1H NMR spectra (500.01 MHz) of symmetric H_2L^4 and its asymmetric mono(amido)gold(III) complex, **4** (inset structure). Signal integrals and peak assignments are based on the schemes for H_2L^4 and **4** given in the Experimental Section. Arrows track the splittings and shifts for protons *a* and *f* that accompany chelation of Au^{III} and the loss of symmetry in **4** relative to the free ligand. Intramolecular hydrogen bonds and a midrange C–H...π interaction are shown with dashed lines and interaction distances (structure inset). The spectra were recorded in $\text{DMSO}-d_6$ at 303 K.

equivalent amide NH protons of the free ligand resonate farthest downfield (10.90 ppm). The relatively narrow line width (2.33 Hz) of the amide NH signal indicates negligible dynamic proton exchange in solution at ambient temperature (as expected for nonacidic protons). Analysis of the intramolecular hydrogen bonds of H_2L^4 (Figure S2 in the Supporting Information) shows that the amide NH atom H100 is involved in a three-center (bifurcated) hydrogen bond in which the adjacent isoquinoline N (N1) and carbonyl O (O1) atoms act as hydrogen-bond acceptors for the N–H donor. The amide NH atom H200 is hydrogen-bonded to the adjacent isoquinoline atom N4. Even if some rotational exchange of the two isoquinolylamido moieties occurs in solution, the NH protons of H_2L^4 are expected to be rigorously hydrogen-bonded throughout such a process, consistent with an intrinsically narrow line width. Interestingly, the amide NH protons of H_2L^1 and H_2L^2 have broader line widths than that

observed for H_2L^4 and, furthermore, exhibit 1:2:1 triplet patterns indicative of spin–spin coupling to the ^{14}N nucleus.^{48–51} The aromatic nature of the bridge between the amide groups of H_2L^4 presumably negates ^1H – ^{14}N spin coupling in this compound.

As far as the diamagnetic gold(III) complexes are concerned, the ^1H and ^{13}C NMR spectra of **1**–**3** are fully assigned in the Experimental Section and displayed in Figures S14–S19 in the Supporting Information. A more detailed analysis of the ^1H NMR spectrum of the gold(III) complex **4** is given below and in Figure 3 for two reasons: first, the ligand is novel and, second, the solid-state conformation of **4** is evidently maintained in fluid solution, which is of significance when interpreting biological data for this complex in solution. Before closer inspection of the ^1H NMR spectrum of **4**, an important general observation for the metal chelates **1**, **2**, and **4** is that the 2-fold structural and magnetic symmetry of the free ligand is lost upon chelation of the Au^{III} ion by only one of two otherwise equivalent amide groups. This leads to doubling-up of the number independent ^1H and ^{13}C signals for each gold(III) complex relative to the free ligand, with the only exception being the signal from one, as opposed to two, amide NH protons (deprotonation of the metal-bound amide group accounting for the loss of the second amide proton). From Figure 3, it is evident that the amide proton (*k*) in the gold(III) complex exhibits a minor (0.07 ppm) upfield shift relative to the free ligand. More marked, however, is the splitting and dramatic shifts of the isoquinoline α -CH proton resonances (i.e., those adjacent to the isoquinoline N atom, *a* and *q*) upon chelation of the metal ion. From the X-ray structure of **4**, CH proton *a* (atom H1) forms an intramolecular hydrogen bond to the closest chloride ligand (Cl1). The interaction is characterized by the following distances and angle: H1…Cl1, 2.71 Å; C1–H1, 0.95 Å; C1–H1…Cl1, 121.1°. The effect of this particular interaction is marked deshielding of the proton (labeled *a* in both spectral traces), which culminates in a 0.76 ppm downfield shift in the signal for **4** relative to the chemical shift of the proton in the free ligand. The analogous proton on the metal-free isoquinoline group of **4**, proton *q*, is chemically and magnetically distinct from proton *a*. Because of the spatial location of proton *q* directly over the metal-bound isoquinoline ring containing N1 (at a fairly loose ring centroid-to-proton distance of 4.33 Å), proton *q* is shielded by the ring current of the ring system. The magnitude of the upfield shift is 0.52 ppm. Equivalent protons *f* in the free ligand split into two single-integral signals (*f* and *l*) in complex **4**. These protons are only marginally affected by metalation of the ligand, consistent with an essentially unchanged environment relative to the free ligand. The remaining isoquinoline ring protons of **4** split into independent signals consistent with the fact that only one isoquinoline ring serves as a ligand to Au^{III} and all symmetry is lost in the metal complex. For example, metalation splits the 4-fold-degenerate doublet at 8.25 ppm of the free ligand (protons *b* and *e*) into four independent doublets (*b*, *e*, *m*, and *p*); protons *b* and *e* belonging to the metal-bound isoquinoline ring exhibit a \geq 0.23 ppm downfield shift relative to the free ligand and reflect, in broad terms, the effect that polarization of the ring by the metal ion has on ^1H nuclear shielding in the present system.

Interestingly, the signals for the amide NH protons of **1** and **2** (but not **4**) exhibit triplet patterns (1:2:1 intensity ratio) consistent with spin–spin coupling to the ^{14}N nucleus (*I* = 1) of the amide N atom in each case (Figure S20 in the

Supporting Information). The spin–spin coupling constants, $^1J_{\text{HN}}$, are 6.08(2) and 6.19(6) Hz for **1** and **2**, respectively. The line widths of the NH proton resonances of **1** and **2** are comparable, averaging 4.6(4) and 4.9(7) Hz, respectively; both are broader than the Lorentzian line width (2.24 Hz) for the NH proton of **4**. As noted above for H_2L^4 , the lack of ^{14}N – ^1H spin coupling in the case of **4** presumably reflects the effect of the aromatic bridge (benzene ring) between the amide groups, which negates spin coupling (this is certainly the case at 303 K). A final point regarding the NMR spectra for **1**, **2**, and **4** is that time-dependent spectral changes were evident in dimethyl sulfoxide (DMSO). Specifically, complexes **1** and **2** showed clear evidence of demetalation over a period of ca. 1 month (Figure S21 in the Supporting Information), while complex **4** formed an insoluble brown precipitate after 10 days, possibly a new compound or an aggregated species. Compound **3**, on the other hand, was stable.

DFT Simulations and Electronic Spectroscopy. In this section, we describe selected structural and electrostatic data obtained from DFT simulations on **1**–**4** with a specific emphasis on compound **4** (because of its moderate cytotoxicity and thus potential as a prototypical metallodrug candidate). Table 1 compares DFT-calculated bond distances and bond angles for **1**–**4**, notably those of the chelate ring and ligands to Au^{III} , to the analogous structural parameters of the X-ray structures. The mean differences between the calculated and observed bond distances of the ligand donor atoms to the Au^{III} ion of each structure are 0.029(16), 0.037(13), 0.051(6), and 0.037(11) Å for **1**–**4**, respectively. The degree of similitude between the calculated and observed structures is even higher for the C=O and amide N–C bonds of **1**–**4** with the mean differences measuring 0.003(9), 0.001(7), 0.010(7), and –0.018(14) Å, respectively.

A visual comparison of the match between the DFT-calculated and X-ray structures of **4** is shown in Figure 4a. Superposition of the structures by least-squares minimization of the differences between the non-H atoms of the isoquinoline rings, the Au^{III} and Cl[–] ions, as well as the C and N atoms of the amido chelates reflects good agreement between the DFT-calculated and experimental structures (RMSD, 0.0593 Å). (Similar structural agreement is observed for **1**–**3**; Figure S22 in the Supporting Information.) The structural superposition of Figure 4a confirms the accuracy of the DFT method in the first instance and, second, highlights the fact that the conformations of the auxiliary isoquinolylamido moieties in the two structures differ rather significantly. The nonequivalent positioning of the isoquinoline rings may be traced to the fact that the *in vacuo* DFT-calculated structures do not take into account the hydrogen bonding and π stacking between the metal-free isoquinoline rings of the X-ray structure, i.e., conformational perturbations induced by lattice interactions, as discussed above (Figure 2b).

Figure 4b illustrates the NBO-calculated partial charge distribution for **4**. Three features are noteworthy: (1) The fractional charge on the Au^{III} ion (+0.76 e) is high, despite the presence of three anionic ligands and a net charge of zero for the molecule. This localization of positive charge in the molecule is clearly likely to favor electrostatic interactions with electron-rich systems such as the π bonds of heterocyclic nucleobases or the sugar–phosphate backbone of dsDNA as well as increase the polarity of the compound. (2) The presence of the Au^{III} ion evidently polarizes the coordinated amide group and isoquinoline rings relative to those of the

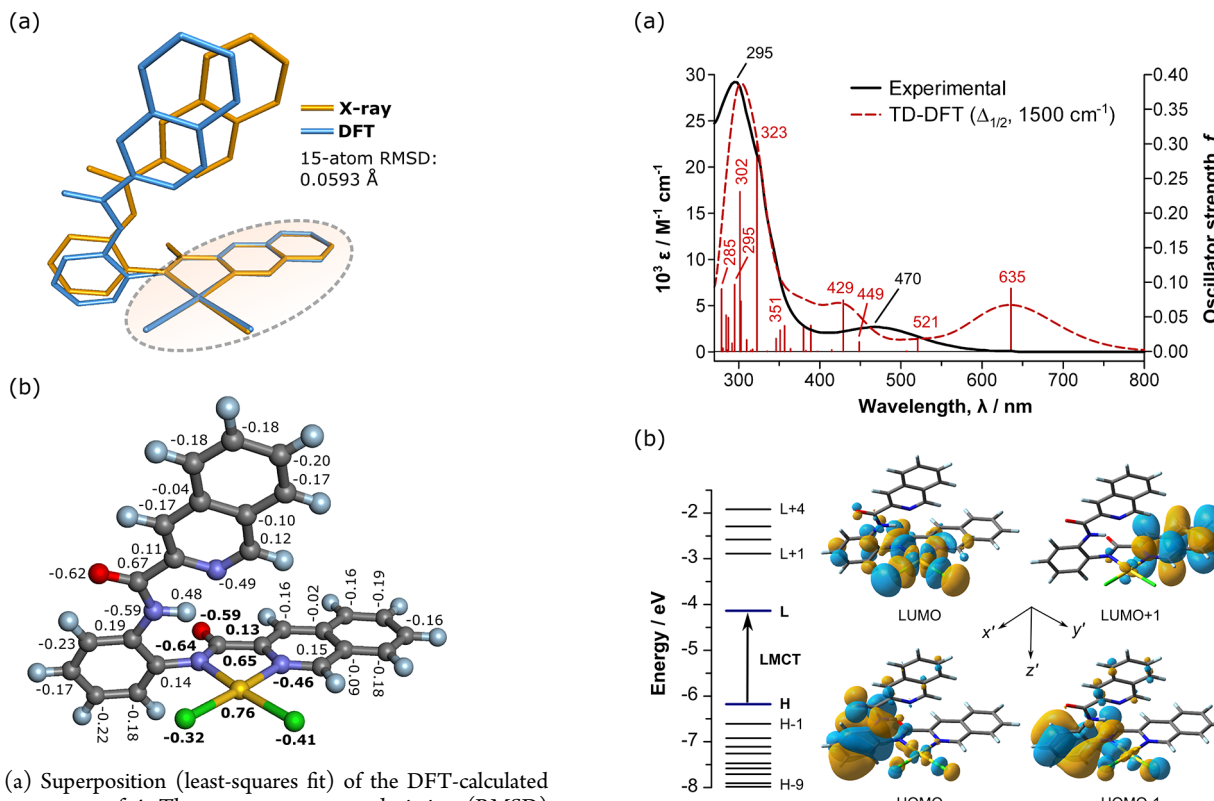


Figure 4. (a) Superposition (least-squares fit) of the DFT-calculated and X-ray structures of **4**. The root-mean-square deviation (RMSD) for the fit (coordination sphere and chelated isoquinolylamido moiety) is indicated. (b) Selected NBO-calculated partial charges for compound **4**. Charges involving the chelate ring and coordinated Cl^- ions are emphasized.

metal-free half of the molecule (partial charge values typically become more positive by up to 0.03 e in the metal-bound isoquinoline ring). (3) The metal-free amide group clearly has both the orientation and partial charge separation to favor hydrogen bonding with suitable partners such as a neighboring molecule in the solid state (e.g., as shown in Figure S12 in the Supporting Information) or suitable biomolecules in living cells. Collectively, complexes **1–4** display similar fractional charge distributions; the partial charges on the metal ion, donor atoms, and amide N, C, and O atoms are essentially equivalent to within 3% of an electron (Table S4 in the Supporting Information). Perhaps the only significant variation in otherwise marginally variant electron populations for the four complexes is the electron density found in the nominally vacant $5d_{x^2-y^2}$ orbital, which measures 1.343, 1.448, 1.330, and 1.637 e for complexes **1–4**, respectively. The somewhat higher electron density for **4** is also reflected in the total $5d$ -orbital electron density, which follows the order **2** (9.203 e) < **3** (9.217 e) \cong **1** (9.218 e) < **4** (9.250 e). These data suggest that the isoquinolylamido chelating ligand of **4** (as opposed to the pyridylamido chelating ligands of **1–3**) is an inherently better σ donor than the less extensively conjugated heterocyclic congener.

Parts a and c of Figure 5 highlight the calculated and experimental electronic spectra of **4** (spectra for **1–3** are available in Figures S23–S25 in the Supporting Information). More specifically, Figure 5a compares the spectrum calculated using time-dependent DFT (TD-DFT)⁷⁷ methods to the experimental spectral envelope; Figure 5b illustrates some of the key molecular orbitals (MOs) involved in the transitions

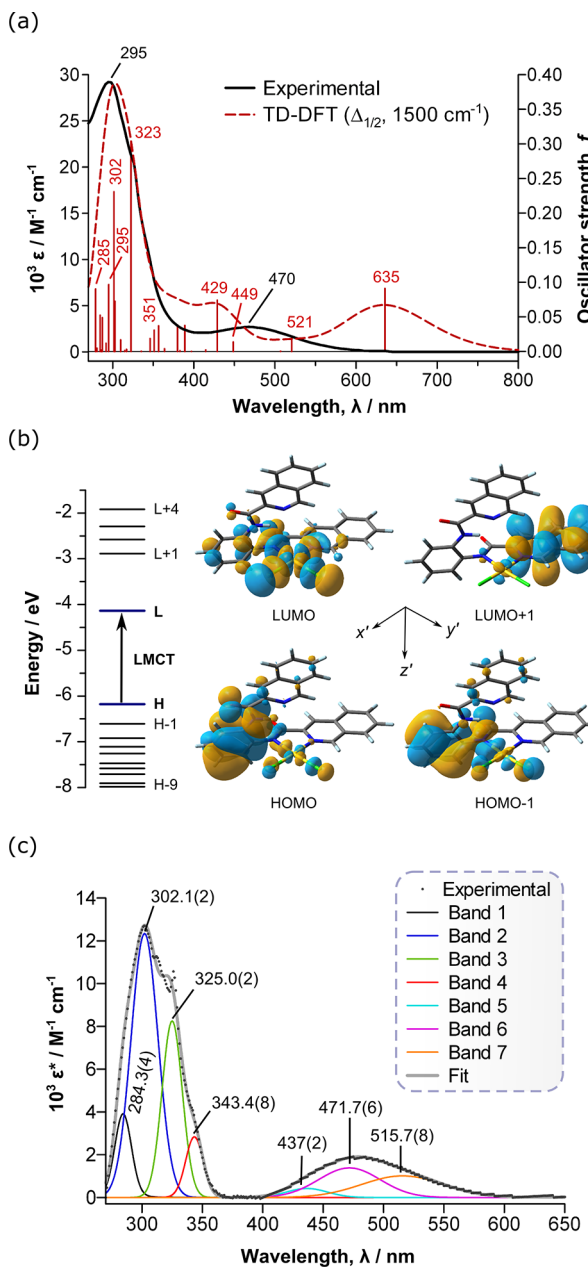


Figure 5. (a) Superposition of the experimental electronic spectrum of **4** (CH_2Cl_2 , 295 K, solid black line) and the TD-DFT-calculated spectrum (30 states, CH_2Cl_2 solvent continuum, broken red line). Calculated states are depicted as vertical lines with intensities given by their oscillator strengths. The DFT-calculated spectral envelope is scaled by a factor of 0.7664 to match the intensity of the experimental spectrum at 295 nm. The LMCT band (lowest-energy transition) has a calculated wavelength of 635 nm. (b) Selected MO energy levels for **4** (left) alongside plots of the four frontier MOs of the complex (right) and the transformed Cartesian axes for assignment of the d-orbital components of each MO. Abbreviations: H, HOMO (MO 135); L, LUMO (MO 136); LMCT, ligand-to-metal charge transfer; $\Delta_{1/2}$, half-width at half-height. (c) Experimental electronic spectrum of **4** from part a deconvoluted into eight constituent Voigt functions after background subtraction ($R^2 = 0.998$). Component band maxima and their standard uncertainties are indicated; band widths and amplitudes are given in Table S6 in the Supporting Information.

that collectively account for the spectrum of the complex, and Figure 6c shows the experimental spectrum of **4** deconvoluted into eight constituent Voigt functions after background

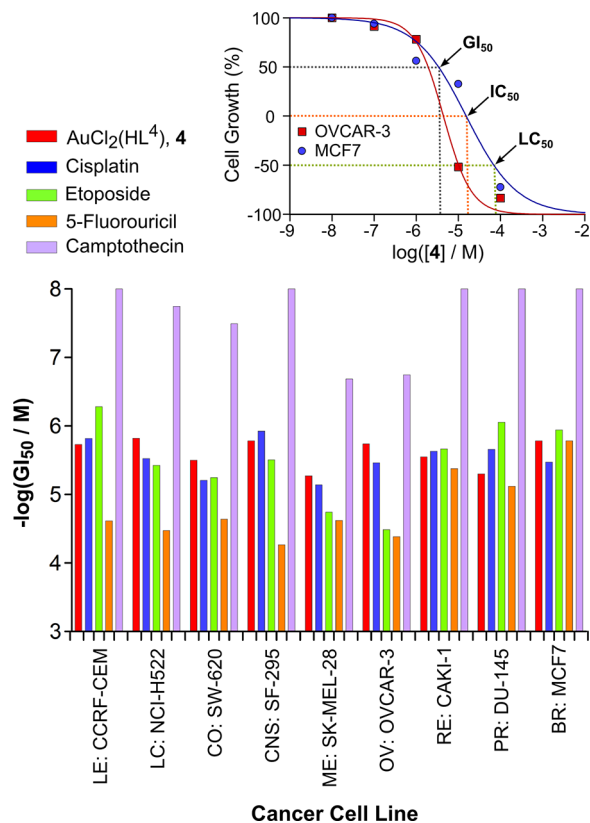


Figure 6. Selected NCI cytotoxicity data for **4** and clinically employed anticancer drugs with known MOAs. The bar chart plots the concentrations at which 50% growth inhibition occurs (GI_{50}) against the human cancer cell line for the indicated compounds. Tall bars correspond to more active growth inhibition by the test agents. The inset illustrates the normalized dose-response profiles for two of the relevant cancer cell lines with compound **4**. Abbreviations: LE, leukemia; LC, nonsmall lung cancer; CO, colon cancer; CNS, central nervous system cancer; ME, melanoma; OV, ovarian cancer; RE, renal cancer; PR, prostate cancer; BR, breast cancer.

subtraction. Transition assignments for the more important excited states of **4** are listed in Table S5 in the Supporting Information. As a whole, the electronic spectra for gold(III) compounds **1–4** are characterized by one or more intense $\pi \rightarrow \pi^*$ bands between 270 and 330 nm and multiple, weaker ligand-to-metal charge-transfer (LMCT) bands in the region 330–600 nm. The agreement between the DFT-calculated and experimental spectra is best for compounds **3** and **4**, with the notable exception of the lowest-energy LMCT band (HOMO \rightarrow LUMO), which is uniformly predicted to be more intense and of longer wavelength (by as much as 150 nm in the case of **3**) than the experimental band profile. Refocusing on compound **4**, parts a and c of Figure 5 indicate that the calculated transition energies for **4** closely match the experimental spectrum below 330 nm in the region dominated by intraligand $\pi \rightarrow \pi^*$ transitions (with the caveat that the calculated intensities are ca. 23% higher than those measured experimentally). Notably, the calculated transition energies involving the excited states with the largest oscillator strengths (302 and 323 nm) fall within 2 nm of the band maxima for the peaks deduced by deconvolution of the experimental spectrum of the complex (bands 2 and 3). Similarly, the lower-intensity deconvoluted bands at 284 and 343 nm (bands 1 and 4) in the experimental spectrum match the energies of the weaker $\pi \rightarrow \pi^*$, $\pi \rightarrow \text{d}\sigma^*$, and $\pi \rightarrow \pi^*/\text{d}\pi^*$ transitions clustered at 285 and 346 nm in the calculated spectrum.

The DFT-calculated and experimental electronic spectra of **4** (and compounds **1–3** in general) are, however, poorly matched in the visible region (making definitive band assignments somewhat more difficult). The problem is that the experimental spectrum of **4** is characterized by a rather broad and featureless absorption envelope that maximizes at ca. 470 nm (Figure 5a); this maximum is without a DFT-calculated counterpart and, as shown by the deconvoluted band profile in Figure 5c, comprises at least three main transitions (437, 472, and 516 nm; bands 5–7, respectively). The two more intense components labeled band 6 (472 nm) and band 7 (516 nm) most probably correspond to the two most intense visible-region LMCT bands of the calculated spectrum (429 and 635 nm), both of which involve excitations from π -symmetry MOs localized on the ligand framework to the LUMO comprising mainly the $5d_{x^2-y^2}$ orbital and σ^* components on the ligand donor atom sets. If the lowest-energy band in the experimental spectrum (516 nm) corresponds to the HOMO \rightarrow LUMO transition, then it is clear that the DFT-calculated energy of this band is too low by a rather substantial 119 nm. The DFT-calculated LMCT transition at 429 nm is then 43 nm too high in energy relative to the experimental band with sufficient intensity to match this assignment at 472 nm (i.e., band 6). Despite these obvious disagreements between the calculated and experimental electronic spectra of **4** and the ensuing difficulty in assigning the experimental bands, it is noteworthy that the three bands that make up the visible-region spectra of **4** have band widths, $\Delta_{1/2}$, that are ≥ 1.5 times broader than those determined for the $\pi \rightarrow \pi^*$ bands below 370 nm in the spectrum. This observation coupled with the molar absorptivities of the visible bands ($\epsilon > 1000 \text{ M}^{-1} \text{ cm}^{-1}$) confirms their LMCT character.

NCI Cytotoxicity Screens. Compounds **2–4** were accepted for initial single-dose NCI-60 cytotoxicity screens (10^{-5} M test agent concentration) by the NCI (Bethesda, MD); compound **1** was not selected owing to its structural homology with **2**. Of the three compounds screened, only **4** was sufficiently cytotoxic in the single-dose assay to warrant a full five-dose NCI screen spanning the concentration range 10^{-8} – 10^{-4} M. (Cytotoxicity data for **2–4** over the NCI's panel of 60 human cancer cell lines are available in the Supporting Information.) From the one-dose screens, the mean growth percentages were 105, 97, and 60% for compounds **2–4**, respectively. From the five-dose screen of **4**, the lowest IC_{50} values were for the ovarian cancer cell lines OVCAR-3 (4.0 μM) and IGROV1 (9.8 μM) and the colon cancer cell line SW-620 (15 μM). Figure 6 compares the best GI_{50} values for compound **4** with analogous data for clinically deployed anticancer drugs that have definitive MOAs. Mean cytotoxicity parameters for compound **4** obtained for each of the nine classes of human cancer in the NCI-60 screen are listed in Table 3. Collectively, the data indicate that colon and ovarian cancer cell lines are, on average, the most susceptible to the gold(III) complex with GI_{50} and IC_{50} values below 10 and 20 μM , respectively. Several noteworthy points emerge from the comparative data of Figure 6: (1) The cytotoxicity of **4** compares favorably with that of cisplatin (a DNA cross-linking agent and guanine-N7 binder) and etoposide (a nonintercalating topoisomerase II, Top2, poison). (2) With the exception of CPT, neither **4** nor any of the other drugs exhibit low nanomolar GI_{50} values. The growth inhibition data for **4**, both

Table 3. Summary of Cytotoxicity Parameters for Compound 4 from a Five-Dose Screen against the NCI's Panel of 60 Human Cancer Cell Lines^a

cancer	N	GI ₅₀ /μM	IC ₅₀ /μM	LC ₅₀ /μM
leukemia	6	13(10)	24(18)	>100
lung	9	11(4)	31(11)	92(77)
colon	7	8.9(2.7)	13(4)	85(68)
CNS	6	11(4)	32(17)	86(70)
melanoma	8	14(5)	27(15)	>100
ovarian	7	7.2(2.5)	18(6)	60(24)
renal	8	8.6(2.6)	21(10)	66(44)
prostate	2	8.3(4.1)	19(10)	70(42)
breast	6	7.7(2.8)	26(10)	87(71)
average	59 ^b	10(4)	23(11)	78(57)

^aAbbreviations: N, number of cell lines within each cancer category; GI₅₀, compound concentration effecting 50% growth inhibition; IC₅₀, compound concentration effecting 100% growth inhibition; LC₅₀, compound concentration that induces 50% cell death. ^bTotal number of cell lines used. Estimated standard deviations are given in parentheses; large values indicate variable susceptibility of a specific group of cell lines to the test compound (see Table S7 in the Supporting Information).

on average and for the most sensitive cancer cell lines, therefore do not compare favorably with the ultrahigh cytotoxicity displayed by CPT (the archetypal Top1 poison). (3) A commercially successful anticancer compound need not have submicromolar GI₅₀ values. For example, 5-fluorouracil displays only moderate cytotoxicity (the GI₅₀ values for many cell lines exceed 10 μM), yet the drug is a widely prescribed antineoplastic antimetabolite.^{78,79} As noted above, the NCI's panel of seven ovarian cancer cell lines was the most sensitive to 4. Upon further reflection, 4 behaves similarly to the structurally related *cis*-dichlorogold(III) dithiocarbamates reported by Ronconi et al.,²⁷ with both compound classes exhibiting IC₅₀ values in the low micromolar range for ovarian cancer.

An important question is whether the GI₅₀ values acquired in the NCI-60 screen for a compound with an unknown MOA may be used to statistically delineate a probable MOA or cellular target for the compound. We have used hierarchical cluster analysis (Figure 7) with the set of GI₅₀ values for 4 and several anticancer drugs with well-known MOAs to determine a likely target for 4 in vivo. As highlighted in Figure 7, compound 4 is equivalent to zorubicin, a human topoisomerase II α (Top2) poison, and, moreover, clusters with the topoisomerase IB (Top1) poisons topotecan, 9-methoxycamptothecin, and CPT. The statistical data therefore strongly suggest that compound 4 exerts its cytotoxic effect by inhibiting Top2 and/or Top1. Note that despite 4 having some structural similarity to cisplatin (a pair of *cis*-chloride ligands bound to a d⁸ transition-metal ion), the compound exhibits a cytotoxicity profile *dissimilar* to that of cisplatin. One reason for this is that the chloride ligands in 4 are substitution-inert, reducing the likelihood of aquation of the metal ion under physiological conditions and thus subsequent coordination of the gold(III) complex to DNA.

Confirmation of the molecular MOA of compound 4 implied by the hierarchical cluster analysis requires that *in vitro* enzyme inhibition assays with both Top1 and Top2 be conducted in the first instance. Because topoisomerase inhibitors may be divided into IFPs (interfacial poisons; drugs that irreversibly trap DNA–enzyme covalent complexes) and CICs (catalytic

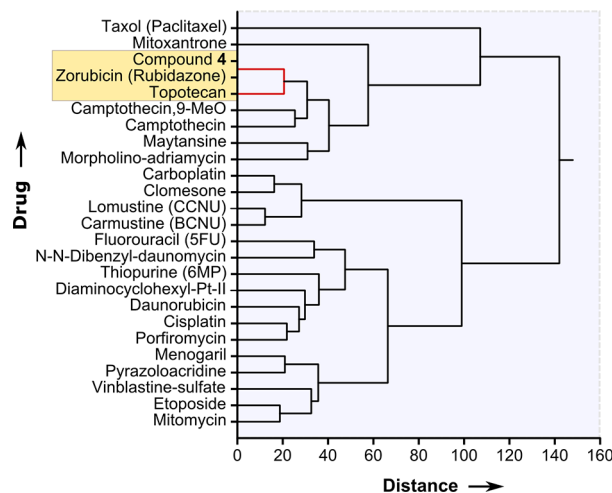


Figure 7. Multivariate hierarchical cluster analysis of the $-\log(\text{GI}_{50})$ data from the NCI-60 screen of compound 4 and 24 anticancer compounds with known *in vivo* targets. The dendrogram was produced using the group average method (average linkages) and Minkowski distances.

inhibitors; drugs that inhibit the enzyme by noncovalent binding of the protein or the enzyme's target DNA sequence), experimental methods capable of delineating between the two types of MOAs ultimately need to be used.

Topoisomerase II α Inhibition Assays. Because 4 targets Top2 (Figure 7), we have used a Top2 enzyme inhibition assay (equivalent to that developed and marketed by TopoGEN, Inc.) to gauge the dose–response function for the test agent with the target enzyme. The agarose gel shown in Figure 8a clearly indicates that concentrations of $[4] < 50 \text{ nM}$ result in essentially undetectable quantities of linear DNA cleavage product and do not inhibit decatenation of kDNA by Top2. However, for [4] in the range of 50 nM to 1 μM (lanes 8–11), there is a clear nonlinear increase in the amount of linear DNA with increasing gold(III) chelate concentration. The dose–response function maximizes at $[4] = 1 \mu\text{M}$ before commencing a nonlinear decrease with increasing [4] over the range of 5–50 μM (lanes 12–15). The overall dose–response function is therefore biphasic with a skewed bell-like shape. The bell-shaped dependence of the linear DNA product concentration upon increasing [4] is well-fitted by eq 2 (Experimental Section), a simple summation of two consecutive opposing (positive and negative) dose–response functions. The first binding event, marked by its midpoint A on the graph, has $K_{D1} \sim 240 \text{ nM}^2$ and a Hill coefficient, n_{H1} , of 2.4(7) (i.e., ~ 2 within 1σ). The Hill coefficient of 2 is consistent with two binding sites for the gold(III) complex in the first equilibrium.⁸⁰ The second binding event, midpoint B on the graph, has $K_{D2} \sim 8.6 \mu\text{M}$ and a Hill coefficient, n_{H2} , of 1.2(2), with the latter value for the Hill coefficient reflecting a single binding site for 4 in the second equilibrium.

The biphasic dose–response function, dual-equilibrium dissociation constants, and Hill coefficients above clearly signify a switch in the reaction mechanism from compound 4 behaving as an IFP at low concentrations to the compound operating as a CIC at higher concentrations. Mechanistically, the first phase is consistent with two molecules of 4 noncovalently binding to an intermediate Top2–DNA covalent cleavage complex at its two nick sites (K_{D1}) in a manner akin to that recently elucidated for etoposide (VP-16) from the X-ray structure of the quaternary

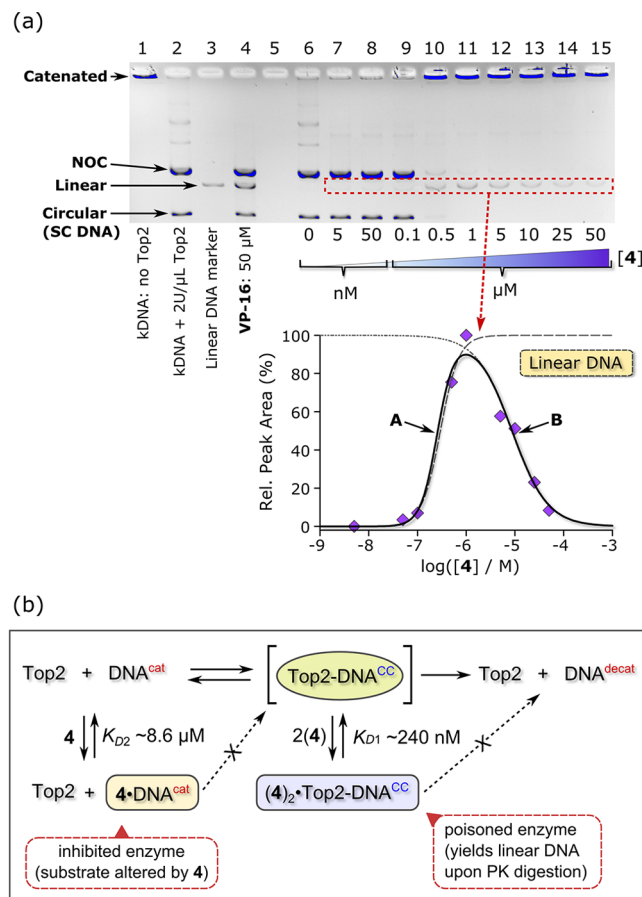


Figure 8. (a) Electrophoretic analysis (1% agarose gel, 0.5 $\mu\text{g mL}^{-1}$ ethidium bromide, EB) of a topoisomerase II (Top2) decatenation assay employing kinetoplast DNA (kDNA, 200 ng μL^{-1} , 30 ng well $^{-1}$) as the substrate, an enzyme concentration of 2 units (U) per μL , etoposide (VP-16) as the Top2 poison control, and compound 4 as the test agent over a broad concentration range. All annotated lanes, unless otherwise indicated, contain Top2. The inset plots the relative peak areas (proportional to the concentration) for the highlighted linear DNA bands. The solid line shows a fit of the dose–response data to eq 2. (Independent functions fitting parts A and B of the skewed bell-shaped curve are shown as broken gray lines.) (b) Biphasic inhibition of Top2 by 4. The normal catalyzed reaction of Top2 runs from left to right: Top2 forms a covalent cleavage complex (Top2-DNA^{CC}) with catenated DNA (DNA^{cat}) as the substrate, allowing the passage of a remote DNA strand through the double-stranded break in the covalently anchored DNA within the cleavage complex. Top2 reseals the cleaved DNA strand prior to release of circular DNA. Repetition of the reaction converts catenated DNA into decatenated DNA (DNA^{decat}), with the latter comprising supercoiled (SC) and nicked-open-circular (NOC) DNA. Compound 4 behaves as an IFP that traps the covalent cleavage complex at low concentrations (section A of the dose–response curve, K_{D1}). At higher concentrations of 4 (section B of the dose–response curve, K_{D2}), competitive binding of the gold(III) chelate to the DNA substrate blocks Top2 from recognizing its substrate, leading to catalytic inhibition of the enzyme. Abbreviation: PK, proteinase K.

(drug)₂-DNA–enzyme covalent cleavage complex.⁸¹ Figure 8a shows that, as the concentration of the gold(III) chelate increases from 50 nM to 1 μM , the trapped (i.e., poisoned) fraction of the intermediate DNA–enzyme covalent cleavage complex increases during the catalytic cycle of the enzyme, as expected, accounting for the increase in the amount of linear DNA product isolated from the reaction.

The mechanistic switch with increasing [4] to a second phase requires that the gold(III) chelate has an additional target with a lower binding constant (K_{D2}) than insertion of the compound at the Top2–DNA cleavage complex nick sites (K_{D1}). As discussed later, 4 binds weakly to DNA, probably by intercalation (but only at higher concentrations), and it is therefore conceivable that weak intercalative binding at (or near) the DNA base sequence targeted by Top2 as [4] increases competes with nick-site binding and ultimately dominates (by preventing the enzyme from associating with its substrate) at elevated concentrations of the gold(III) chelate. In effect, catalytic inhibition of Top2 wins out over poisoning of the enzyme at higher concentrations of 4 such that the yield of linear reaction product declines for [4] > 1 μM (lanes 11–15). Note that catalytic inhibition of Top2 becomes clearly evident even at [4] = 500 nM (lane 10) because the yield of NOC DNA is markedly reduced at this concentration. Furthermore, untransformed catenated DNA (nonmigrating in 1% agarose gel) has sharply accumulated in the well, a pattern that becomes even more marked in the 1–50 μM concentration range for 4 (lanes 11–15). On the basis of the published catalytic mechanism for Top2⁸² and the crystal structure of the VP-16-poisoned enzyme,⁸¹ a simplified mechanistic scheme (Figure 8b) may be used to adequately account for the present data.

Dual-mode IFP catalytic inhibitors of Top2 with hallmark bell-shaped dose–response curves have been reported by others, e.g., with compounds such as 9-hydroxyellipticine⁸³ and adriamycin (doxorubicin),^{84,85} but often the data are not suitable for the quantification of stepwise K_D values as we have been able to do with 4. Our interpretation of the dual-mode reaction of 4 with Top2 is thus consistent with earlier viewpoints on similar biphasic inhibition of the enzyme with polycyclic organic compounds. Moreover, the enzyme inhibition data fully support the MOA of 4 identified from the *in vivo* cytotoxicity data (GI_{50} values) by hierarchical cluster analysis.

Topoisomerase IB Inhibition Assays. Hierarchical cluster analysis of the NCI data for 4 (Figure 7) showed that, in addition to being equivalent to zorubicin (a Top2 IFP), 4 behaves *similarly* (not identically) to topotecan, a Top1 IFP. The most widely used Top1 inhibition assay gauges the ability of Top1 to relax SC plasmid DNA with increasing drug concentration. However, with a possible mixed mode of inhibition (IFP and CIC), the standard assay is complicated by the fact that 4 is also a DNA intercalator, as described below. As a result, the topoisomer distribution of reaction products is altered by the test drug, which complicates data interpretation. As detailed in the Experimental Section, we have modified the standard Top1 inhibition assay so that it may be used to distinguish between an IFP and a catalytic inhibitor of Top1. The new assay is based on the fact that, at low salt concentrations and high enzyme loadings, the probability of forming a 2:1 (Top1)₂-DNA covalent cleavage complex during enzyme turnover increases. In the presence of an IFP of the enzyme, which traps the covalent cleavage complexes by binding at the enzyme-bound nick sites on adjacent DNA strands, the fraction of doubly nicked DNA present in the system will increase. Upon quenching of the reaction followed by PK digestion to remove covalently bound Top1 from the DNA, this yields an increase in the fraction of linear DNA in the reaction product mixture (provided that some of the nick sites on adjacent strands are close enough that the circular DNA opens up to its linear form with fairly short, nonannealing

sticky ends). In essence, under these assay conditions, the activity of Top1 is substantially enhanced, significantly increasing the probability of trapping the cleavage intermediate, even in the absence an IFP. To prove that the cleavages we detect are due to Top1, a control with CPT (Figure 9, lane 5) shows that this potent IFP results in double-stranded DNA breaks because of the nested action of Top1 molecules. In support of this, previous work showed that endogenous Top1 has the ability to "cluster" at catalytic sites on genomic DNA in situ;⁸⁶ thus, at high input levels of enzyme in the presence of an IFP like CPT, nested single-stranded DNA cleavages give rise to double-stranded breaks.

Figure 9 shows the reaction products generated in this modified Top1 inhibition assay. Lane 2 of the EB gel indicates that Top1 relaxes pHOT1 plasmid DNA in the absence of an added inhibitor to give a heightened concentration of NOC DNA and relaxed-circular DNA (RX DNA), as expected from our working hypothesis above. In the presence of a high concentration of a known and potent Top1 IFP (50 μM CPT, lane 5), only NOC DNA and linear DNA are obtained from the reaction. (RX DNA is absent because of complete poisoning of Top1 at this dose of the control compound.)

Lanes 7–13 reflect the reaction products with increasing concentrations of 4 up to 25 μM ; at no point is linear DNA evident. Notably, the yield of NOC DNA decreases in a sigmoidal fashion as [4] increases, while the fraction of untransformed SC DNA substrate increases with the sigmoidal mirror image curve. The assay clearly identifies 4 as a catalytic inhibitor of Top1 with a K_D or IC_{50} value of ca. 4 μM .

Overview of the MOA of 4. The Top2 and Top1 enzyme inhibition assays (Figures 8 and 9) indicate that 4 targets both DNA-regulating enzymes in similar, yet different ways. Catalytic inhibition through DNA binding (see below) is evidently the common catalytic inhibition mechanism for both Top1 and

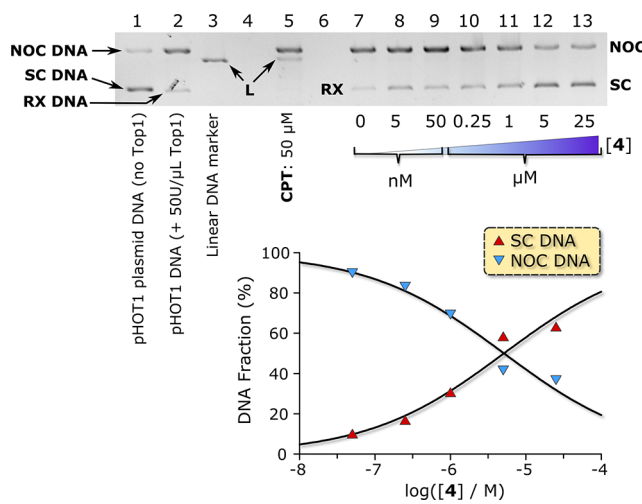


Figure 9. Electrophoretic analysis of a “zero-salt, enzyme-rich” topoisomerase IB (Top1) cleavage assay employing SC plasmid DNA (pHOT1, 188 ng μL^{-1}) as the substrate, an enzyme concentration of 50 U μL^{-1} (in all annotated lanes except the first), CPT as the Top1 poison control, and compound 4 over a wide concentration range, maximizing at 25 μM . The inset plots the relative concentrations of NOC and SC DNA in lanes 9–13. The gel (1% agarose) contains EB (0.5 $\mu\text{g mL}^{-1}$). Abbreviations: L, NOC, SC, and RX represent linear, nicked-open circular, supercoiled, and relaxed DNA, respectively.

Top 2 (with K_D values in the micromolar range). The ability of 4 to act as an IFP of Top2 at low concentrations (K_D in the nanomolar range) is, however, unique to its mode of action with Top2. This likely reflects the specific three-dimensional constraints of the pair of nick sites in the Top2–DNA covalent cleavage complex,⁸¹ which evidently fit the structure of 4 yet are different from the single nick site of the Top1–DNA cleavage complex.⁷⁴ Despite having obtained X-ray structural data for 4 (vide supra) and an understanding of the compound’s ability to form π – π stacks, speculation as to how 4 might intercalate at the nick sites of the Top2–DNA cleavage complex is unwarranted with the data at hand. Interestingly, Wang et al.⁸⁷ recently reported a series of cationic and neutral platinum(II) poly(pyridine) complexes with acetylides nucleobases as variable coligands that were either Top2 or dual Top2/Top1 inhibitors. Changes in the ligand structure modulated both the activity level and mechanism of inhibition (IFP or CIC) of Top2 by the compounds. In the present study, 4 evidently behaves similarly to the above platinum(II) complexes.

DNA Binding by 4. From the reactions of 4 with Top1 and Top2, catalytic inhibition of both enzymes at $[4] > 1 \mu\text{M}$ appears to reflect binding of the compound to the enzyme’s DNA substrate (in a fashion similar to that of doxorubicin and its analogues).⁸⁴ We employed electrophoretic mobility shift assays (EMSA) with pHOT1 plasmid DNA and varying concentrations of 4, EB (a cationic DNA intercalator control), and *m*-AMSA (a neutral DNA intercalator control⁸⁸) to test this hypothesis and to further investigate the interaction of 4 with DNA. In these experiments, the plasmid DNA substrate was equilibrated with the test compounds for 15 min at 37 °C in essentially the same buffer solution as that used for the Top1 and Top2 inhibition assays. The gel in Figure 10a shows that both plasmid DNA bands (SC DNA, form I; NOC DNA, form II) exhibit reduced mobility with increasing concentrations of both EB and 4. The SC DNA band (form I) is affected most by intercalation of EB and by the binding of 4, with compound 4 inducing a 6% mobility shift of SC DNA at a concentration of 50 μM (Figure 10b). In comparison, the cationic DNA intercalator control compound (EB) engenders a 21% mobility shift of SC DNA at a concentration of 50 μM . The marked difference in the magnitude of the mobility shift for the SC DNA band probably reflects several factors including the charge differences for the two compounds, their intrinsic DNA binding affinities, the extent and sites of intercalation, as well as their inherently different structures.

We tested the hypothesis that the charge of the DNA intercalator is important in determining the magnitude of the mobility shift by performing the analogous EMSA for *m*-AMSA, a neutral DNA intercalator control compound (Figure 10d,e). This compound had the smallest effect (3.9% shift) on the mobility of SC DNA, and the band broadening observed with EB and 4 was virtually absent. One interpretation of this result is that, although 4 is overall a neutral compound, it does contain the Au^{III} cation, which, as shown by our DFT simulations, retains a fractional positive charge of ca. 0.76 e on the Au^{III} center, making it polar and thus allowing it to have a similar (but understandably smaller) effect on the topology (and thus mobility) of SC DNA relative to the cationic intercalator EB. In a nutshell, the results displayed in Figure 10 suggest that 4 weakly intercalates DNA at relatively high concentrations (>5 μM) and that this likely underpins catalytic inhibition of Top1 and Top2 by the compound. Interestingly,

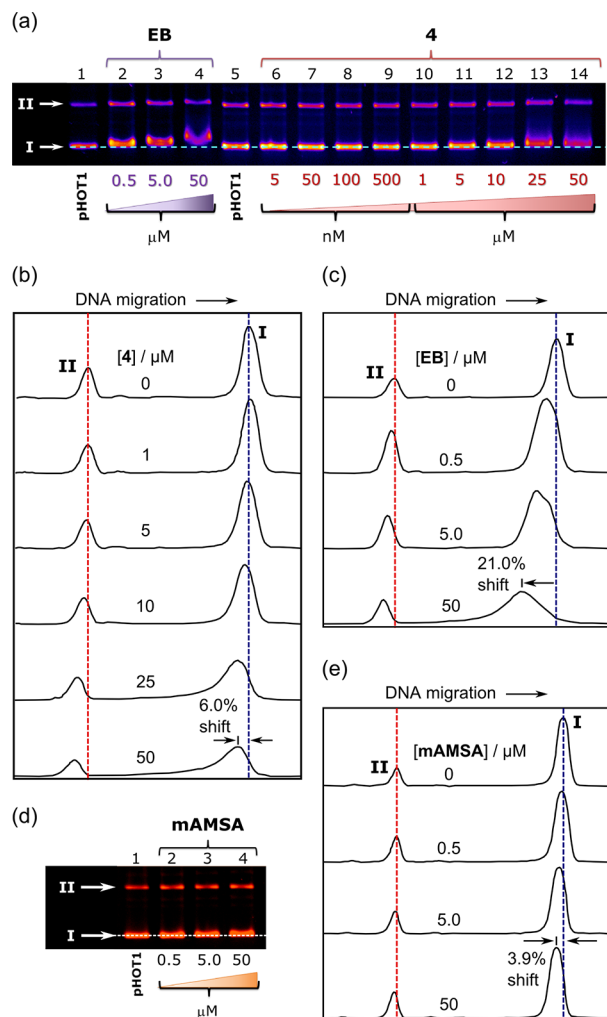


Figure 10. (a) EMSA of double-stranded pHO7.1 plasmid DNA as a function of the concentration of **4** and the cationic DNA intercalator EB control. DNA band identities: I, SC DNA; II, NOC DNA. (b) Two-dimensional peak deconvolution of lanes 5 and 10–14 of the gel shown in part a. (c) Two-dimensional peak deconvolution of lanes 1–4 of the gel shown in part a. (d) EMSA of double-stranded pHO7.1 plasmid DNA as a function of the concentration of the neutral DNA intercalator *m*-AMSA [*m*-amsacrine or 4'- (acridinylamino)-methanesulfon-*m*-aniside]. (e) Two-dimensional peak deconvolution of lanes 1–4 of the gel shown in part d.

DNA-intercalating cytotoxic gold(III) porphyrins also inhibit Top1, but a definitive mechanism is still lacking.²³

With all DNA-binding compounds, the question arises as to whether the compound is an intercalator or a groove binder. There are different ways to answer this question, with one of the simplest (other than an EMSA) being a DNA winding assay.⁸⁹ In this experiment (Figure S29 in the Supporting Information), fully relaxed plasmid DNA was equilibrated with **4** prior to reaction with Top1. As highlighted by Palchaudhuri and Hergenrother,⁸⁹ a DNA intercalator will bind to the relaxed plasmid DNA generated by the action of Top1 and then induce negative supercoiling of the substrate. In the case of a strong DNA intercalator, this ideally results in the appearance of topoisomer bands on the gel with increasing intercalator concentration and ultimately only SC DNA at the highest compound dose. Nonintercalative compounds yield a negative result in the assay. From the data in Figure S29 in the

Supporting Information, it is clear that DNA-bound **4** induces partial negative supercoiling of relaxed pHO7.1 plasmid DNA in the presence of Top1. This confirms that **4** is a weaker DNA intercalator than EB but, nonetheless, an intercalator capable of catalytically inhibiting both Top1 and Top2. Importantly, because not all DNA intercalators inhibit these DNA-regulating enzymes, we conclude that **4** must intercalate, even if only partially, at a base pair at or near the target base sequences recognized by Top1 and Top2.

Stability of **4 in Biological Buffers.** The moderate cytotoxicity of **4** *in vivo* (Table 3) suggests that the loss of **4** to physical, chemical, or cellular (e.g., drug efflux) processes might lower its effective concentration over the time course of cell growth experiments. From the time-dependent decrease in the absorbance at 295 nm for **4** (Figure S30 in the Supporting Information; pH 7.34, 37 °C), the monomeric gold(III) complex clearly undergoes slow, biphasic precipitation. The process commences after a ca. 5–6 h induction period and is essentially complete after 48 h. Notably, the rate constants were independent of the NaCl concentration (from 35.5 to 1000 mM); the averaged values were $k_1 = 0.184(6)$ h⁻¹ and $k_2 = 3.4(1.6) \times 10^{-3}$ h⁻¹. Importantly, hydrolysis of the Au–Cl bonds of **4** appears *not* to occur for two reasons: (1) such a process would show a dependence on [NaCl], contrary to observation, and (2) substitution of the chloride ligands bound to the Au^{III} ion would be expected to shift the LMCT bands in the electronic spectrum. Our spectral data are consistent with the Au–Cl bonds of **4** remaining intact for more than 72 h in solution. Similar solution stability was recently reported for *cis*-dichlorogold(III) derivatives of 2-(2'-pyridyl)benzimidazole.⁹⁰ That said, on the time scale of the NCI's cytotoxicity screens (48 h), precipitation of **4** will compete with cellular uptake of the compound and may ultimately lower the effective cytotoxicity of the compound.

CONCLUSIONS

In summary, and before enumerating the key conclusions of this work, four neutral AuCl₂(X) derivatives **1–4**, where X is an anionic bidentate pyridyl- or quinolylamido chelate, were synthesized and characterized by X-ray diffraction, DFT simulations, and a range of spectroscopic techniques. Compounds **2–4** were screened for their cytotoxicity against the NCI's panel of 60 human cancer cell lines and the MOA of the most active compound (quinolylamido chelate **4**) elucidated using statistical methods coupled with *in vitro* enzyme inhibition assays. DNA and topoisomerases IB and II α are the principal cellular targets of the compound.

The main conclusions of this study are the following. (1) Although the ligands for **1**, **2**, and **4** are potentially tetradequate, they fail to substitute all four Cl[−] ions when reacted with [AuCl₄][−] salts, leading to bidentate *cis*-dichlorogold(III) complexes. (2) Compounds **1–4** exhibit a significant structural trans effect induced by the amido N donor, which favors elongation of the diametric Au–Cl bond in each case. (3) DFT calculations showed that significant residual fractional cationic charge resides on the Au^{III} ions of **1–4** (ca. +0.8 e), which is evidently important for the interaction of **4** with DNA. (4) Compound **4** was moderately cytotoxic in a five-dose NCI-60 screen (mean IC₅₀ over 60 cell lines ~38 μM). (5) Hierarchical cluster analysis methods indicated that **4** is mechanistically *equivalent* to the doxorubicin analogue zorubicin, a Top2 poison, and mechanistically *similar* to topotecan, a Top1 poison. (6) Using a Top2 inhibition assay, we have shown that

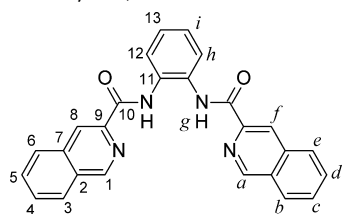
4 is an IFP of Top2 at low concentrations ($K_D \sim 240$ nM) and a catalytic inhibitor of the enzyme at higher concentrations ($K_D \sim 9 \mu\text{M}$). (7) A new enzyme inhibition assay capable of distinguishing between IFPs and catalytic inhibitors of Top1 was developed and used to prove that **4** is a catalytic inhibitor, but not an IFP, of Top1. (8) Last, catalytic inhibition of Top1 and Top2 by **4** evidently reflects DNA intercalation by the compound. Going forward, structural derivatives or formulations (e.g., micelles) of **4** less susceptible to precipitation from aqueous solutions may have improved cytotoxicity and thus prospects for further development.

EXPERIMENTAL SECTION

General Procedures. All reagents were used as received from Aldrich unless otherwise stated. All reactions were carried out under atmospheric conditions. Pyridine, methanol, dimethyl sulfoxide (DMSO), and nitromethane were Chromosolve HPLC-grade solvents. Dichloromethane (DCM) was distilled over calcium hydride. Gold pellets were received as a loan from Mintek (Randburg, South Africa) as part of project AuTEK Biomed. Electronic spectra were recorded with a Shimadzu UV-1800 spectrometer (2 nm slit width) using varying solvents in 1.0-cm-path-length quartz cuvettes. Fourier transform infrared spectra were obtained on a Bruker Alpha spectrometer (36 scans, spectral resolution = 1.0 cm^{-1}) with a diamond ATR accessory for studying microcrystalline samples. ^1H and ^{13}C NMR spectra were recorded using saturated solutions in DMSO- d_6 or chloroform- d_1 using either a 500 MHz Bruker Avance III spectrometer equipped with an 11.7 T magnet and a 5 mm BBO probe or a 400 MHz Bruker Avance III spectrometer equipped with a 9.4 T magnet and a 5 mm BBOF probe. The solvent signal was used as the reference. All spectra were recorded at 303.15 K unless otherwise stated. Proton and carbon signal assignments were made from consideration of the DFT-calculated nuclear shielding tensors (vide infra) in conjunction with the primary experimental NMR spectra (one-dimensional ^1H and ^{13}C , COSY, HSQC, HMBC, DEPT-90, and DEPT-135). KyPlot 5.0.2 (KyensLab, Inc.)⁹¹ was used for all graphing and curve-fitting. Fitky 0.9.8 was used for spectral peak deconvolution and envelope fitting.⁹²

Ligand Synthesis. The free ligands HL^1 , H_2L^2 , and H_2L^3 were prepared according to literature procedures and gave consistent spectroscopic data.^{48–51}

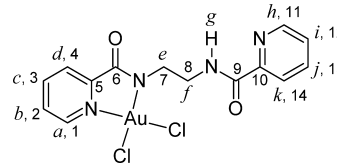
Ligand H_2L^4 . To a solution of isoquinolinecarboxylic acid (2.00 g, 1.624×10^{-2} mol) in dry pyridine (15 mL) was added 1,2-diaminobenzene (0.878 g, 8.122×10^{-3} mol) in pyridine (5 mL). The mixture was stirred for 5 min, during which time a white precipitate formed. The mixture was then heated to 110 °C prior to the dropwise addition of triphenylphosphite (5.041 g, 1.624×10^{-2} mol), which was followed by continuous stirring at 110 °C for 4 h. The solution was then allowed to cool and stand overnight, during which time the product (*N,N'*-benzene-1,2-diylisoquinoline-3-carboxamide, H_2L^4) crystallized out of solution. The product was isolated by filtration and washed with diethyl ether (2 × 25 mL) and distilled water (2 × 25 mL) to obtain a white powder. X-ray-quality crystals were obtained by diffusion of diethyl ether into a saturated solution of H_2L^4 in DCM. Yield: 65% (colorless crystals).



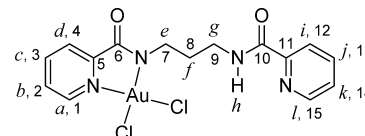
TOF MS ES: m/z 419.1507 (calcd, m/z 419.1508), M^+ . Anal. Calcd for $\text{C}_{26}\text{H}_{18}\text{N}_4\text{O}_2$: C, 74.63; H, 4.34; N, 13.39. Found: C, 74.73; H, 4.46; N, 13.57. UV-vis [CH_2Cl_2 ; λ_{max} nm (ϵ , $\text{M}^{-1} \text{cm}^{-1}$)]: 232.5 (1.6 × 10⁵), 289 (4.6 × 10⁴), 310 (3.4 × 10⁴), 324.5 (2.8 × 10⁴). IR (powder, cm^{-1}): 3337 (s, $\nu(\text{N}-\text{H})$, R-NH-COR), 1689 (s, $\nu(\text{CO})$,

RNH-CO-R). ^1H NMR (500 MHz, DMSO- d_6 , 303.15 K): δ 10.90 (s, 2H, g), 9.36 (s, 2H, a), 8.73 (s, 2H, f), 8.25 (d, 4H, J = 9.0 Hz, e, b), 7.90 (ddd, 2H, J_1 = 9.4 Hz, J_2 = 4.3 Hz, J_3 = 1.2 Hz, d), 7.87 (dd, 2H, J_1 = 5.9 Hz, J_2 = 3.6 Hz, h), 7.82 (ddd, 2H, J_1 = 9.3 Hz, J_2 = 4.3 Hz, J_3 = 1.1 Hz, c), 7.33 (dd, 2H, J_1 = 6.0 Hz, J_2 = 3.6 Hz, i). ^{13}C NMR (123 MHz, DMSO- d_6 , 303.15 K): δ 163.62 (C-10), 152.13 (C-1), 143.76 (C-9), 135.91 (C-11), 132.01 (C-5), 131.67 (C-7), 129.92 (C-4), 129.89 (C-2), 128.59 (C-3), 128.37 (C-6), 126.07 (C-12), 125.68 (C-13), 121.04 (C-8).

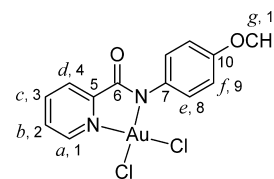
General Synthetic Procedure for Metal Complexes. A solution of the ligand (5.29×10^{-4} mol) in DCM (15 mL) was added to a solution of $\text{K}[\text{AuCl}_4]$ (5.29×10^{-4} mol) in methanol (10 mL). This solution was then stirred while sodium acetate (6.00×10^{-4} mol) in methanol (10 mL) was added dropwise prior to heating the reaction under reflux for 2 h. The solution was then cooled to room temperature and allowed to stir overnight to afford an orange-red precipitate, which was filtered off and washed with methanol (2×10 mL).



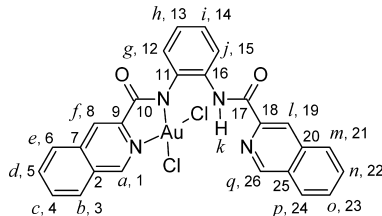
$\text{AuCl}_2(\text{HL}^1)$, **Compound 1.** *cis*-Dichloro{(pyridin-2-ylcarbonyl)[2-[(pyridin-2-ylcarbonyl)amino]ethyl]azanido}gold(III). Yield: 72% (orange powder). TOF MS ES: m/z 558.9976 (calcd, m/z 558.9979), [(M + Na)⁺]. Anal. Calcd for $\text{C}_{14}\text{H}_{13}\text{AuCl}_2\text{N}_4\text{O}_2$: C, 31.30; H, 2.44; N, 10.43. Found: C, 30.95; H, 2.42; N, 10.16. UV-vis [DMSO; λ_{max} nm (ϵ , $\text{M}^{-1} \text{cm}^{-1}$)]: 312 (5.1 × 10³), 453 (1.4 × 10²). IR (powder, cm^{-1}): 3360 (s, $\nu(\text{N}-\text{H})$, R-NH-COR), 1645 (s, $\nu(\text{CO})$, RNH-CO-R), 1602 (s, $\nu(\text{CO})$, RN-CO-R). ^1H NMR (400 MHz, DMSO- d_6 , 303.15 K): δ 9.32 (d, 1H, J = 3.04 Hz, a), 8.88 (t, 1H, J = 6.08(2) Hz, g), 8.56 (d, 1H, J = 2.04 Hz, k), 8.48 (t, 1H, J = 7.64 Hz, c), 8.03 (t, 1H, J = 6.82 Hz, b), 7.92 (m, 3H, d, h, i), 7.54 (m, 1H, j), 3.72 (t, 2H, J = 5.42 Hz, e), 3.57 (m, 2H, f). ^{13}C NMR (100 MHz, DMSO- d_6 , 303.15 K): δ 171.66 (C-6), 164.73 (C-9), 150.60 (C-11), 149.40 (C-10), 148.70 (C-5), 145.51 (C-1), 145.31 (C-3), 138.06 (C-2), 130.33 (C-4), 128.65 (C-14), 126.73 (C-13), 122.19 (C-12), 46.35 (C-7), 40.23 (C-8).



$\text{AuCl}_2(\text{HL}^2)$, **Compound 2.** *cis*-Dichloro{(pyridine-2-yl-carbonyl)[3-[(pyridin-2-ylcarbonyl)amino]propyl]azanido}gold(III). Yield: 78% (orange powder). TOF MS ES: m/z 573.0134 (calcd, m/z 573.0135), [(M + Na)⁺]. Anal. Calcd for $\text{C}_{15}\text{H}_{15}\text{AuCl}_2\text{N}_4\text{O}_2$: C, 32.69; H, 2.74; N, 10.16. Found: C, 32.57; H, 2.69; N, 10.02. UV-vis [DMSO; λ_{max} nm (ϵ , $\text{M}^{-1} \text{cm}^{-1}$)]: 310 (3.9 × 10³), 449 (1.2 × 10²). IR (powder cm^{-1}): 3392 (s, $\nu(\text{N}-\text{H})$, R-NH-COR), 1666 (s, $\nu(\text{CO})$, RNHCO-R), 1643 (s, $\nu(\text{CO})$, RN-CO-R). ^1H NMR (400 MHz, DMSO- d_6 , 303.15 K): δ 9.29 (d, 1H, J = 2.85 Hz, a), 8.81 (t, 1H, J = 6.19(6) Hz, h), 8.61 (m, 1H, i), 8.50 (t, 1H, J = 7.72 Hz, b), 8.00 (m, 4H, c, d, k, l), 7.58 (m, 1H, j), 3.56 (m, 2H, e), 3.36 (m, 2H, g), 1.86 (m, 2H, f). ^{13}C NMR (100 MHz, DMSO- d_6 , 303.15 K): δ 170.96 (C-6), 163.55 (C-10), 149.95 (C-15), 148.82 (C-11), 148.28 (C-5), 145.03 (C-1), 144.91 (C-3), 137.77 (C-13), 129.82 (C-2), 128.18 (C-4), 126.34 (C-14), 121.72 (C-12), 44.49 (C-7), 36.31 (C-9), 29.94 (C-8).



$\text{AuCl}_2(L^3)$, Compound 3, *cis*-Dichloro[(4-methoxyphenyl)(pyridin-2-ylcarbonyl)azanido]gold(III). Yield: 69% (dark red powder). TOF MS ES: *m/z* 494.9947 (calcd, *m/z* 494.9941), M^+ . Anal. Calcd for $C_{13}H_{11}\text{AuCl}_2\text{N}_4\text{O}_2$: C, 31.54; H, 2.24; N, 5.66. Found: C, 31.73; H, 2.10; N, 5.32. IR (powder cm^{-1}): 2947, 3063, 3105 (s, $\nu(\text{CH})$, OCH_3), 1643 (s, $\nu(\text{CO})$, RN-CO-R). UV-vis [CH_2Cl_2 ; λ_{max} nm (ϵ , $\text{M}^{-1} \text{cm}^{-1}$)]: 265 (9.5 $\times 10^3$), 333 (4.9 $\times 10^3$), 400 (3.3 $\times 10^3$), 470 (3.3 $\times 10^3$). ^1H NMR (400 MHz, DMSO-*d*₆, 303.15 K): δ 9.36 (d, 1H, *J* = 2.86 Hz, a), 8.55 (t, 1H, *J* = 7.73 Hz, c); 8.08 (m, 2H, b, d), 7.20 (m, 2H, e), 6.91 (m, 2H, f), 3.78 (s, 3H, g). ^{13}C NMR (100 MHz, DMSO-*d*₆, 303.15 K): δ 169.83 (C-6), 158.26 (C-10), 148.26 (C-5), 144.98 (C-1), 144.98 (C-3), 137.14 (C-7), 130.04 (C-8), 130.01 (C-2), 128.44 (C-4), 113.36 (C-9), 55.24 (C-11).



$\text{AuCl}_2(\text{HL}^4)$, Compound 4. The same general procedure used above was employed for the synthesis of 4, *cis*-dichloro{[isoquinolin-3-ylcarbonyl][2-[isoquinolin-3-ylcarbonyl]amino]phenyl}azanido]gold(III). However, the postmetalation reaction mixture was filtered and the filtrate allowed to evaporate to dryness in a beaker to afford solid 4 as well as an unidentified byproduct. The solid product was dissolved in DCM and the insoluble byproduct removed by filtration. The solution of 4 in DCM was layered in test tubes with diethyl ether to afford clean 4 as a dark-red powder. X-ray-quality crystals were obtained by the slow diffusion of diethyl ether into a saturated solution of 4 in nitromethane. Yield: 30% (dark-red powder). TOF MS ES: *m/z* 685.0463 (calcd, *m/z* 685.0472), M^+ . Anal. Calcd for $C_{26}H_{17}\text{AuCl}_2\text{N}_4\text{O}_2$: C, 45.57; H, 2.50; N, 8.18. Found: C, 45.81; H, 2.61; N, 8.03. IR (powder cm^{-1}): 3324 (s, $\nu(\text{N}-\text{H})$, R-NH-COR), 1668 (s, $\nu(\text{CO})$, RNH-CO-R), 1652 (s, $\nu(\text{CO})$, RN-CO-R). UV-vis [CH_2Cl_2 ; λ_{max} nm (ϵ , $\text{M}^{-1} \text{cm}^{-1}$)]: 240 (1.2 $\times 10^5$), 247 (1.0 $\times 10^5$), 295 (3.0 $\times 10^4$), 326 (2.2 $\times 10^4$), 470 (2.9 $\times 10^3$). ^1H NMR (500.013 MHz, DMSO-*d*₆, 303.15 K): δ 10.85 (s, 1H, k), 10.33 (s, 1H, a), 9.10 (s, 1H, q), 8.86 (d, 1H, j), 8.84 (s, 1H, l), 8.69 (s, 1H, f), 8.53 (d, 1H, *J* = 8.14 Hz, b), 8.48 (d, 1H, *J* = 8.00 Hz, e), 8.29 (t, 1H, *J* = 7.75 Hz, c), 8.22 (d, 1H, *J* = 8.14 Hz, m), 8.15 (t, 1H, *J* = 7.61 Hz, i), 8.12 (d, 1H, *J* = 8.24 Hz, p), 7.88 (t, 1H, *J* = 7.49 Hz, n), 7.78 (t, 1H, *J* = 7.54 Hz, o), 7.48 (d, 1H, *J* = 7.93 Hz, g), 7.47 (t, 1H, *J* = 7.50 Hz, d), 7.22 (t, 1H, *J* = 7.74 Hz, h). ^{13}C NMR (100 MHz, DMSO-*d*₆, 303.15 K): δ 170.47 (C-17), 162.13 (C-10), 152.28 (C-26), 150.88 (C-1), 143.40 (C-18), 139.43 (C-9), 137.41 (C-16), 136.75 (C-4), 135.91 (C-11), 135.41 (C-7), 134.31 (C-20), 132.49 (C-14), 132.15 (C-22), 131.78 (C-15), 130.43 (C-5), 130.10 (C-2), 130.01 (C-23), 129.78 (C-25), 129.14 (C-3), 129.11 (C-21), 128.62 (C-24), 128.38 (C-19), 128.37 (C-12), 124.15 (C-13), 120.75 (C-8), 119.79 (C-6).

X-ray Crystallography. Single crystals of H_2L^4 and 1–4 were epoxy-mounted on glass fibers and used for data collection on an Oxford Diffraction Xcalibur2 CCD four-circle diffractometer equipped with an Oxford Instruments CryoJet. The data were collected at room temperature unless otherwise stated, with Mo $\text{K}\alpha$ (λ = 0.71073 Å) radiation at a crystal-to-detector distance of 50 mm using ω scans at θ = 29.389°, with varying exposure times taken at 2.01 kW X-ray power (0.75° frame widths). The data were reduced with the program *CrysAlis RED*⁹³ using outlier rejection, scan speed scaling, and standard Lorentz and polarization correction factors. Unless otherwise stated, direct methods (*SHELXS-97*⁹⁴ running in *Olex2*⁹⁵) were used to solve the structures. All non-H atoms were located in the E map and refined anisotropically with *SHELXL-97*.⁹⁴ H atoms in each of the structures were idealized (riding model) with standard *SHELXL-97* parameters, unless otherwise stated.

X-ray data for H_2L^4 : $C_{26}\text{H}_{18}\text{N}_4\text{O}_2$, fw = 418.44 amu, a = 5.7773 (2) Å, b = 13.3867 (5) Å, c = 26.7245 (9) Å, β = 93.836 (3)°, V = 2062.22 (13) Å³, monoclinic, $P2_1/n$, Z = 4, D_c = 1.348 g cm⁻³, μ = 0.088 mm⁻¹,

T = 296(2) K, R_1 (wR2) = 0.0485 (0.1263) for 3035 unique data with $I > 2\sigma(I)$, R_1 (wR2) = 0.0629 (0.1377) for all 21333 data ($R_{\text{int}} = 0.0378$), goodness of fit (based on F^2) = 1.064.

X-ray data for 1: $C_{14}\text{H}_{13}\text{AuCl}_2\text{N}_4\text{O}_2$, fw = 537.15 amu, a = 7.477 (5) Å, b = 10.210(5) Å, c = 11.023(5) Å, α = 85.443(5)°, β = 79.313(5)°, γ = 72.383(5)°, V = 787.9(7) Å³, triclinic, $P\bar{1}$, Z = 2, D_c = 2.264 g cm⁻³, μ = 9.689 mm⁻¹, T = 296(2) K, R_1 (wR2) = 0.0335 (0.0816) for 3043 unique data with $I > 2\sigma(I)$, R_1 (wR2) = 0.0396 (0.0834) for all 6130 data ($R_{\text{int}} = 0.0402$), goodness of fit (based on F^2) = 1.010.

X-ray data for 2: $C_{15}\text{H}_{15}\text{AuCl}_2\text{N}_4\text{O}_2$, fw = 551.18 amu, a = 11.188(5) Å, b = 10.192(5) Å, c = 15.132(5) Å, β = 93.350(5)°, V = 1722.5(13) Å³, monoclinic, $P2_1/n$, Z = 4, D_c = 2.125 g cm⁻³, μ = 8.866 mm⁻¹, T = 296(2) K, R_1 (wR2) = 0.0317 (0.0740) for 4240 unique data with $I > 2\sigma(I)$, R_1 (wR2) = 0.0553 (0.0803) for all 6154 data ($R_{\text{int}} = 0.0454$), goodness of fit (based on F^2) = 0.960.

X-ray data for 3: $C_{13}\text{H}_{11}\text{AuCl}_2\text{N}_2\text{O}_2$, fw = 495.10 amu, a = 12.971(5) Å, b = 8.701(5) Å, c = 14.068(5) Å, β = 114.723(5)°, V = 1442.2(11) Å³, monoclinic, $P2_1/n$, Z = 4, D_c = 2.280 g cm⁻³, μ = 10.572 mm⁻¹, T = 296(2) K, R_1 (wR2) = 0.0361 (0.0990) for 2494 unique data with $I > 2\sigma(I)$, R_1 (wR2) = 0.0403 (0.1018) for all 14511 data ($R_{\text{int}} = 0.0451$), goodness of fit (based on F^2) = 1.051.

X-ray data for 4-OEt₂: $C_{26}\text{H}_{17}\text{AuCl}_2\text{N}_4\text{O}_2 \cdot \text{C}_4\text{H}_{10}\text{O}$, fw = 759.42 amu, a = 15.990(5) Å, b = 12.445(5) Å, c = 15.602(5) Å, β = 104.487(5)°, V = 3006.0(18) Å³, monoclinic, $P2_1/c$, Z = 4, D_c = 1.678 g cm⁻³, μ = 5.109 mm⁻¹, T = 100(2) K, R_1 (wR2) = 0.0393 (0.0904) for 7698 unique data with $I > 2\sigma(I)$, R_1 (wR2) = 0.0595 (0.0961) for all 45814 data ($R_{\text{int}} = 0.0577$), goodness of fit (based on F^2) = 0.955.

Molecular Simulations. All DFT calculations were performed using the multiprocessor version of *Gaussian 09W*⁹⁶ with the HSEH1PBE^{97,98} hybrid functional and the 6-311G(d,p) basis set^{99,100} for all atoms except Au, for which the Los Alamos effective core potential basis set LanL2DZ^{101,102} was implemented. An f-type polarization function on Au (α = 0.20) was additionally incorporated. Spectral properties were calculated with standard procedures in *Gaussian 09W*. Specifically, NMR shielding tensors were determined by GIAO theory^{103,104} with DMSO as the solvent (self-consistent-field reaction method based on the conductor-like polarizable continuum model^{105,106}). Electronic spectra were calculated using the TD-DFT method (analytical gradients)^{107,108} with 30 excited states in a DCM solvent continuum. Partial atomic charges were calculated using the natural population analysis routine of NBO version 3.¹⁰⁹

NCI Cytotoxicity Screens. Compounds 2–4 were accepted by the NCI (Bethesda, MD) for single-dose screens at a concentration of 10^{-5} M against their panel of 60 different human tumor cell lines, enabling growth percentages of each cell line to be determined in the presence of the test compounds. Compound 4 proceeded further to a five-dose NCI-60 screen spanning the concentration range of 10^{-8} – 10^{-5} M, allowing the determination of GI_{50} , TGI, and LC_{50} values for the compound. The methodology followed and definitions of the foregoing cytotoxicity parameters are available on the NCI's Developmental Therapeutics Program (DTP) web site.¹¹⁰ The set of 60 GI_{50} values measured for 4 were compared (in negative log format) to the analogous publicly available DTP data for 25 well-known anticancer drugs that have established MOAs. More specifically, the data were analyzed using *KyPlot*⁹¹ with a statistical multivariate cluster analysis algorithm (group average method, Minkowski distances) to calculate a dendrogram on which the analyzed set of anticancer drugs cluster according to similarities in their GI_{50} profiles and thus MOAs.

Topoisomerase II Inhibition Assay. Human topoisomerase II α (Top2) catalyzed dsDNA decatentation reactions were performed with purified kinetoplast DNA (kDNA) and purified enzyme (TopoGEN Inc., Port Orange, FL) following the manufacturer's published method. The resulting agarose gels were destained in deionized water for 15 min and imaged with UV transillumination (302 nm) on a Syngene ChemGenius system followed by quantification and analysis with *ImageJ* 1.46r.¹¹¹

The variation in the linear DNA product concentration as a function of the logarithm of [4] was analyzed using the dual dose-response function below, eq 2,

$$y = 100 \left[\frac{1}{1 + \left(\frac{10^C}{K_{D1}} \right)^{n_{H2}}} - \frac{1}{1 + \left(\frac{10^C}{K_{D1}} \right)^{n_{H1}}} \right] \quad (2)$$

where y is proportional to the concentration of linear DNA reaction product(s) (represented as % abundance relative to the DNA band with the largest area on the gel), C is the molar concentration of 4, and K_{D1} and K_{D2} are the drug or ligand equilibrium dissociation constants for the first and second consecutive inhibition steps, respectively. As lucidly pointed out by Prinz,⁸⁰ the above K_D values are equivalent to IC_{50} values (inhibitor concentrations giving 50% inhibition) for the enzyme. The associated Hill coefficients for the two steps are n_{H1} and n_{H2} ; these coefficients give the number of ligands bound in each step and thus the number of binding sites per enzyme or macromolecular target, *provided that* (i) the reaction is in a dilute solution with $[enzyme] \ll [inhibitor]$ so that the enzyme concentration does not affect the K_D values,¹¹² (ii) the inhibitor is nonaggregating over the concentration range of the study,¹¹³ and (iii) the inhibitor does not operate by nonspecific allosteric denaturation of the enzyme.⁸⁰ The nonlinear least-squares fit of the experimental data to eq 1 (Figure 9a) had the following optimized parameters: K_{D1} , $2.4(1.1) \times 10^{-7} M^2$; n_{H1} , $2.5(7)$; K_{D2} , $8.6(1.5) \times 10^{-6} M$; n_{H2} , $1.2(3)$; $R^2 = 0.987$.

Topoisomerase I Inhibition Assay. Inhibition of Top1-catalyzed relaxation of negatively supercoiled pHOT1 plasmid DNA was studied by two methods: (1) conventional DNA unwinding assays as designed, marketed, and distributed by TopoGEN Inc. and (2) a new DNA cleavage assay contrived to discriminate between a Top1 catalytic inhibitor and a Top1 IFP. The basis of this new method is simple: at low NaCl concentrations and elevated Top1 concentrations (typically 10 times higher than those employed in a standard Top1 inhibition assay), Top1–DNA covalent cleavage complexes with a higher than 1:1 stoichiometry are favored. This results in elevated levels of NOC DNA product when plasmid DNA is used as the substrate in the absence of a Top1 poison. In the presence of a Top1 poison, elevated levels of NOC DNA and linear DNA (normally absent in a standard Top1 inhibition assay) are observed. The linear DNA product in this case arises from cleavages that occur in close proximity on *both strands* of the DNA substrate ostensibly caused by a 2:1 enzyme–DNA stoichiometry at the hexadecameric Top1 cleavage site that is engineered into the pHOT1 plasmid substrate. Because Top1 poisons trap the covalent cleavage intermediates in the catalytic cycle of the enzyme, Top1 IFPs are identifiable by high levels of both NOC and linear DNA reaction products. In contrast, catalytic inhibitor compounds (CICs) do not trap the intermediate covalent DNA–enzyme cleavage complexes and merely lead to dose-dependent reduction of the yield of NOC DNA. Importantly, CICs are distinguished by the absence of linear DNA products in this assay.

Cleavage reactions were carried out in 1 mL polyethylene microcentrifuge tubes with 50 U μL^{-1} of Top1 (TopoGEN, Inc.) and 188 ng μL^{-1} of supercoiled pHOT1 plasmid DNA (TopoGEN, Inc.) in a master mix of 1X TGS buffer [100 mM Tris-HCl, pH 8.0, 10 mM ethylenediaminetetraacetic acid (EDTA), 1 mM spermidine, 1% bovine serum albumin, 5% glycerol, and 0 mM NaCl] at a total initial volume of 29 μL . To each of these solutions was added a 1.0 μL aliquot of an appropriate standard solution of 4 dissolved in molecular biology grade DMSO (Sigma). Final concentrations of 4 ranged from 5 nM to 25 μM in a final reaction volume of 30 μL . Two controls were included: (1) a reaction in the presence of 50 μM CPT (Top1 IFP) and (2) a zero-drug control (1.0 μL of DMSO added to 29 μL of the master mix). Reactions were prepared on ice and initiated by incubation for 30 min at 37 °C. Following incubation, reactions were stopped by the addition of 3.0 μL of 10% sodium dodecyl sulfate and digested with proteinase K (0.5 mg mL^{-1}) for 30 min at 37 °C. To each solution was added 6 μL of 6X DNA electrophoresis loading dye (50% aqueous glycerol and 0.025% bromophenol blue) prior to brief

vortex mixing. A 5.0 μL aliquot of each solution was pipetted into a precast 1% EB–agarose gel (to give 20 ng of DNA per lane) prior to electrophoresis at 50 V for 1 h in a 1X TBE-EB buffer. (Both the gel and electrophoresis buffer contained EB at a final concentration of 0.5 mg mL^{-1} ; this permits optimal resolution of DNA cleavage products.) The gel was briefly destained and imaged as described above (Top2 inhibition assay).

DNA Binding Assay. The significant cytotoxicity profile of 4 and the presence of isoquinoline groups in its structure (i.e., known DNA intercalator groups) warranted an assessment of its DNA binding affinity. Standard spectroscopic titrations of the metal complexes with calf-thymus DNA in phosphate-buffered 5% DMSO solutions (pH 7.0, 25 °C) gave irreproducible binding isotherms. EMSAs were required to reproducibly detect an interaction between 4 and DNA. For these experiments, 6.3 ng μL^{-1} of negatively supercoiled pHOT1 plasmid DNA (TopoGEN, Inc.) was used as the dsDNA substrate. Reaction solutions were prepared by mixing 1.0 μL of a 188 ng μL^{-1} pHOT1 stock solution, 3.0 μL of pH 7.9 1X TGS buffer [100 mM Tris-HCl, 10 mM EDTA, 1.5 M NaCl, 1 mM spermidine, 1% BSA, and 50% (v/v) glycerol], and 25.0 μL of deionized water in 1 mL polyethylene microcentrifuge tubes. To these solutions were added 1.0 μL aliquots of standard solutions of EB (a cationic DNA intercalator control) or *m*-AMSA (a neutral DNA intercalator control) in DMSO (molecular biology grade, Sigma) to give final control compound concentrations of 500 nM, 5.0 μM , and 50 μM . For 4, additions of 1.0 μL aliquots of appropriate freshly made standard solutions of the test compound in DMSO were made to an analogous series of pHOT1-containing reaction solutions (29.0 μL total volumes) to give final compound concentrations ranging from 5.0 nM to 50 μM . The solutions were incubated at 37 °C for 15 min before adding 6.0 μL of a 6X electrophoresis loading dye (50% aqueous glycerol and 0.025% bromophenol blue) and mixing by vortex centrifugation. Aliquots from each dyed solution (5.0 μL) were loaded on a freshly cast 1% agarose gel and electrophoresed in 1X TBE buffer (88 mM boric acid, 88 mM Tris base, 10 mM EDTA, pH 7.8) at 50 V for 60 min. The gel was rinsed in deionized water and stained for 10 min in an aqueous 1X TBE-buffered EB solution (0.5 $\mu g mL^{-1}$) prior to imaging as described above (Top2 inhibition assay).

ASSOCIATED CONTENT

Supporting Information

Figures S1–S30 containing additional crystallographic and spectroscopic data as well as one-dose NCI cytotoxicity screens for 1–3 (five-dose data for 4 are included as an addendum), Tables S1–S7 listing further structural, DFT, and spectroscopic data for one or more of 1–4, and final X-ray crystallographic models in a multipart CIF file. This material is available free of charge via the Internet at <http://pubs.acs.org>.

AUTHOR INFORMATION

Corresponding Author

*E-mail: munroo@ukzn.ac.za.

Author Contributions

C.R.W. synthesized and characterized the compounds and wrote parts of the Experimental Section and draft manuscript; A.M.F. and W.R. performed the topoisomerase assays; O.Q.M. performed the EMSAs; M.T.M. directed the molecular biology experiments; O.Q.M. produced the figures, wrote the final manuscript, and directed the chemistry. All authors have given their approval of the final version of the manuscript.

Notes

The authors declare no competing financial interest.

ACKNOWLEDGMENTS

O.Q.M. and C.R.W. thank the University of KwaZulu-Natal for facilities and funding. C.R.W. thanks the NRF (South Africa)

for a Ph.D. bursary. Special thanks go to AuTEK Biomed (Dr. Judy Coates) for providing significant financial resources for running this project over several years and for seeding the foundations of our current metallodrug discovery initiative at UKZN. A.M.F., W.R., and M.T.M. thank the University of Central Florida (UCF) for research facilities and funding. Furthermore, all authors thank TopoGEN, Inc. (Port Orange, FL), for kindly providing purified enzymes, *k*DNA, plasmid DNA, and assay kits that made the pivotal molecular biology component of this study possible. O.Q.M. extends his deepest gratitude to the NCI (Bethesda, MD), specifically the DTP, for their expert cytotoxicity screening service and to Craig Grimmer (UKZN) for all of his help with the NMR experiments. Finally, O.Q.M. thanks the Fulbright Association for a 2011–2012 Visiting Fulbright Scholarship to the USA and M.T.M. for his friendship and generosity while hosting him at UCF.

■ REFERENCES

- Rosenberg, B.; Vancamp, L.; Krigas, T. *Nature* **1965**, *205*, 698–699.
- Sherman, S. E.; Gibson, D.; Wang, A. H.; Lippard, S. J. *Science* **1985**, *230*, 412–417.
- Coll, M.; Sherman, S. E.; Gibson, D.; Lippard, S. J.; Wang, A. H. *J. Biomol. Struct. Dyn.* **1990**, *8*, 315–330.
- Ziegler, C. J.; Silverman, A. P.; Lippard, S. J. *J. Biol. Inorg. Chem.* **2000**, *5*, 774–783.
- Kelland, L. *Expert Opin. Investig. Drugs* **2007**, *16*, 1009–1021.
- Hannon, M. J. *Pure Appl. Chem.* **2007**, *79*, 2243–2261.
- Schiller, J. H.; Harrington, D.; Belani, C. P.; Langer, C.; Sandler, A.; Krook, J.; Zhu, J.; Johnson, D. H. N. *Engl. J. Med.* **2002**, *346*, 92–98.
- Lovejoy, K. S.; Lippard, S. J. *Dalton Trans.* **2009**, 10651–10659.
- Kelland, L. *Nat. Rev. Cancer* **2007**, *7*, 573–584.
- Guo, Z. J.; Sadler, P. J. *Adv. Inorg. Chem.* **2000**, *49*, 183–306.
- Guo, Z. J.; Sadler, P. J. *Angew. Chem., Int. Ed.* **1999**, *38*, 1513–1531.
- Ronconi, L.; Marzano, C.; Zanello, P.; Corsini, M.; Miolo, G.; Macca, C.; Trevisan, A.; Fregona, D. *J. Med. Chem.* **2006**, *49*, 1648–1657.
- Milacic, V.; Chen, D.; Ronconi, L.; Landis-Piwowar, K. R.; Fregona, D.; Dou, Q. P. *Cancer Res.* **2006**, *66*, 10478–10486.
- Shaw, C. F. *Chem. Rev.* **1999**, *99*, 2589–2600.
- Calamai, P.; Carotti, S.; Guerri, A.; Mazzei, T.; Messori, L.; Mini, E.; Orioli, P.; Speroni, G. P. *Anti-Cancer Drug Des.* **1998**, *13*, 67–80.
- Gabbiani, C.; Casini, A.; Messori, L. *Gold Bull.* **2007**, *40*, 73–81.
- Abbate, F.; Orioli, P.; Bruni, B.; Marcon, G.; Messori, L. *Inorg. Chim. Acta* **2000**, *311*, 1–5.
- Casini, A.; Hartinger, C.; Gabbiani, C.; Mini, E.; Dyson, P. J.; Keppler, B. K.; Messori, L. *J. Inorg. Biochem.* **2008**, *102*, 564–575.
- Casini, A.; Messori, L. *Curr. Top. Med. Chem.* **2011**, *11*, 2647–2660.
- Gabbiani, C.; Casini, A.; Messori, L.; Guerri, A.; Cinelli, M. A.; Mlnghetti, G.; Corsini, M.; Rosani, C.; Zanello, P.; Arca, M. *Inorg. Chem.* **2008**, *47*, 2368–2379.
- Messori, L.; Abbate, F.; Marcon, G.; Orioli, P.; Fontani, M.; Mini, E.; Mazzei, T.; Carotti, S.; O'Connell, T.; Zanello, P. *J. Med. Chem.* **2000**, *43*, 3541–3548.
- Che, C. M.; Sun, R. W.; Yu, W. Y.; Ko, C. B.; Zhu, N.; Sun, H. *Chem. Commun.* **2003**, 1718–1719.
- Sun, R. W. Y.; Li, C. K. L.; Ma, D. L.; Yan, J. J.; Lok, C. N.; Leung, C. H.; Zhu, N. Y.; Che, C. M. *Chem.—Eur. J.* **2010**, *16*, 3097–3113.
- Pitteri, B.; Marangoni, G.; Visentin, F.; Bobbo, T.; Bertolasi, V.; Gilli, P. *J. Chem. Soc., Dalton Trans.* **1999**, 677–682.
- Hollis, L. S.; Lippard, S. J. *J. Am. Chem. Soc.* **1983**, *105*, 4293–4299.
- Carotti, S.; Marcon, G.; Marussich, M.; Mazzei, T.; Messori, L.; Mini, E.; Orioli, P. *Chem.—Biol. Interact.* **2000**, *125*, 29–38.
- Ronconi, L.; Giovagnini, L.; Marzano, C.; Bettio, F.; Graziani, R.; Pilloni, G.; Fregona, D. *Inorg. Chem.* **2005**, *44*, 1867–1881.
- Kim, J. H.; Everett, G. W. *Inorg. Chem.* **1981**, *20*, 853–856.
- Buckley, R. G.; Elsome, A. M.; Fricker, S. P.; Henderson, G. R.; Theobald, B. R. C.; Parish, R. V.; Howe, B. P.; Kelland, L. R. *J. Med. Chem.* **1996**, *39*, 5208–5214.
- Parish, R. V.; Mack, J.; Hargreaves, L.; Wright, J. P.; Buckley, R. G.; Elsome, A. M.; Fricker, S. P.; Theobald, B. R. C. *J. Chem. Soc., Dalton Trans.* **1996**, 69–74.
- Ortner, K.; Abram, U. *Inorg. Chem. Commun.* **1998**, *1*, 251–253.
- Marcon, G.; Carotti, S.; Coronello, M.; Messori, L.; Mini, E.; Orioli, P.; Mazzei, T.; Cinelli, M. A.; Minghetti, G. *J. Med. Chem.* **2002**, *45*, 1672–1677.
- Parish, R. V.; Howe, B. P.; Wright, J. P.; Mack, J.; Pritchard, R. G.; Buckley, R. G.; Elsome, A. M.; Fricker, S. P. *Inorg. Chem.* **1996**, *35*, 1659–1666.
- Wang, Y.; He, Q. Y.; Che, C. M.; Chiu, J. F. *Proteomics* **2006**, *6*, 131–142.
- Wang, Y.; He, Q. Y.; Sun, R. W.; Che, C. M.; Chiu, J. F. *Eur. J. Pharmacol.* **2007**, *554*, 113–122.
- Momekov, G.; Ferdinandov, D.; Konstantinov, S.; Arpadjan, S.; Tsekova, D.; Gencheva, G.; Bontchev, P. R.; Karaivanova, M. *Bioinorg. Chem. Appl.* **2008**, 367471.
- Wang, Y.; He, Q. Y.; Che, C. M.; Tsao, S. W.; Sun, R. W.; Chiu, J. F. *Biochem. Pharmacol.* **2008**, *75*, 1282–1291.
- To, Y. F.; Sun, R. W.; Chen, Y.; Chan, V. S.; Yu, W. Y.; Tam, P. K.; Che, C. M.; Lin, C. L. *Int. J. Cancer* **2009**, *124*, 1971–1979.
- Sun, R. W.; Li, C. K.; Ma, D. L.; Yan, J. J.; Lok, C. N.; Leung, C. H.; Zhu, N.; Che, C. M. *Chemistry* **2010**, *16*, 3097–3113.
- Yan, J. J.; Chow, A. L.; Leung, C. H.; Sun, R. W.; Ma, D. L.; Che, C. M. *Chem. Commun.* **2010**, *46*, 3893–3895.
- Li, C. K. L.; Sun, R. W. Y.; Kui, S. C. F.; Zhu, N. Y.; Che, C. M. *Chem.—Eur. J.* **2006**, *12*, 5253–5266.
- Chow, K. H.; Sun, R. W.; Lam, J. B.; Li, C. K.; Xu, A.; Ma, D. L.; Abagyan, R.; Wang, Y.; Che, C. M. *Cancer Res.* **2010**, *70*, 329–337.
- Milacic, V.; Fregona, D.; Dou, Q. P. *Histol. Histopathol.* **2008**, *23*, 101–108.
- Cheung, T. C.; Lai, T. F.; Che, C. M. *Polyhedron* **1994**, *13*, 2073–2077.
- Sun, R. W. Y.; Che, C. M. *Coord. Chem. Rev.* **2009**, *293*, 1682–1691.
- Yang, T.; Tu, C.; Zhang, J. Y.; Lin, L. P.; Zhang, X. M.; Liu, Q.; Ding, J.; Xu, Q.; Guo, Z. J. *Dalton Trans.* **2003**, 3419–3424.
- Yang, T.; Zhang, J. Y.; Tu, C.; Lin, J.; Liu, Q.; Guo, Z. J. *Chin. J. Inorg. Chem.* **2003**, *19*, 45–48.
- Barnes, D. J.; Chapman, R. L.; Vagg, R. S.; Watton, E. C. *J. Chem. Eng. Data* **1978**, *23*, 349–350.
- Munro, O. Q.; Wilson, C. *Acta Crystallogr., Sect. C: Cryst. Struct. Commun.* **2010**, *66*, O535–O539.
- Wilson, C. R.; Munro, O. Q. *Acta Crystallogr., Sect. C: Cryst. Struct. Commun.* **2010**, *66*, o513–o516.
- Dutta, S.; Pal, S.; Bhattacharya, P. K. *Polyhedron* **1999**, *18*, 2157–2162.
- Tamura, M.; Kajikawa, Y.; Azuma, N.; Tani, H.; Tajima, K.; Kanaori, K.; Makino, K.; Takayama, T. *Acta Crystallogr., Sect. C: Cryst. Struct. Commun.* **1999**, *55*, 719–722.
- Hashmi, A. S. K.; Rudolph, M.; Bats, J. W.; Frey, W.; Rominger, F.; Oeser, T. *Chem.—Eur. J.* **2008**, *14*, 6672–6678.
- Fan, D. M.; Yang, C. T.; Ranford, J. D.; Vittal, J. J. *Dalton Trans.* **2003**, 4749–4753.
- Casini, A.; Diawara, M. C.; Scopelliti, R.; Zakeeruddin, S. M.; Gratzel, M.; Dyson, P. J. *Dalton Trans.* **2010**, *39*, 2239–2245.
- Shepherd, R. E.; Proctor, A.; Henderson, W. W.; Myser, T. K. *Inorg. Chem.* **1987**, *26*, 2440–2444.
- Smith, D. W. *Inorg. Chem.* **1978**, *17*, 3153–3156.

- (58) Lin, Z. Y.; Hall, M. B. *Inorg. Chem.* **1991**, *30*, 646–651.
(59) Pearson, R. G. *Inorg. Chem.* **1973**, *12*, 712–713.
(60) Fan, D. M.; Yang, C. T.; Ranford, J. D.; Lee, P. F.; Vittal, J. J. *Dalton Trans.* **2003**, 2680–2685.
(61) Ahmed, E.; Clark, R. J. H.; Tobe, M. L.; Cattalini, L. *J. Chem. Soc., Dalton Trans.* **1990**, 2701–2706.
(62) Bjernemose, J. K.; Raithby, P. R.; Toftlund, H. *Acta Crystallogr., Sect. E* **2004**, *60*, M1719–M1721.
(63) Aleksić, M.; Savic, V.; Popovic, G.; Buric, N.; Kapetanovic, V. J. *Pharmaceut. Biomed.* **2005**, *39*, 752–756.
(64) Hosmane, R. S.; Liebman, J. F. *Struct. Chem.* **2009**, *20*, 693–697.
(65) Nelson, S. M.; Shepherd, T. M. *Inorg. Chem.* **1965**, *4*, 813–&.
(66) Hunter, C. A.; Sanders, J. K. M. *J. Am. Chem. Soc.* **1990**, *112*, 5525–5534.
(67) Janiak, C. *J. Chem. Soc., Dalton Trans.* **2000**, 3885–3896.
(68) Antony, S.; Agama, K. K.; Miao, Z. H.; Hollingshead, M.; Holbeck, S. L.; Wright, M. H.; Varticovski, L.; Nagarajan, M.; Morrell, A.; Cushman, M.; Pommier, Y. *Mol. Pharmacol.* **2006**, *70*, 1109–1120.
(69) Brana, M. F.; Cacho, M.; Garcia, M. A.; de Pascual-Teresa, B.; Ramos, A.; Acero, N.; Llinas, F.; Munoz-Mingarro, D.; Abradelo, C.; Rey-Stolle, M. F.; Yuste, M. *J. Med. Chem.* **2002**, *45*, 5813–5816.
(70) Nitiss, J. L.; Zhou, J.; Rose, A.; Hsiung, Y.; Gale, K. C.; Osheroff, N. *Biochemistry* **1998**, *37*, 3078–3085.
(71) Orhana, I.; Ozcelik, B.; Karaoglu, T.; Sener, B. *Z. Naturforsch. C* **2007**, *62*, 19–26.
(72) Rosenkranz, V.; Wink, M. *Molecules* **2008**, *13*, 2462–2473.
(73) Brana, M. F.; Castellano, J. M.; Moran, M.; Emling, F.; Kluge, M.; Schlick, E.; Klebe, G.; Walker, N. *Arzneimittelforschung* **1995**, *45*, 1311–1318.
(74) Staker, B. L.; Feese, M. D.; Cushman, M.; Pommier, Y.; Zembower, D.; Stewart, L.; Burgin, A. B. *J. Med. Chem.* **2005**, *48*, 2336–2345.
(75) Scott, A. P.; Radom, L. *J. Phys. Chem.* **1996**, *100*, 16502–16513.
(76) Rosenberg, A. *Acta Chem. Scand. A* **1957**, *11*, 1390–1404.
(77) Ahlrichs, R. B. a. R. *Chem. Phys. Lett.* **1996**, *256*, 454–464.
(78) Inada, T.; Ichikawa, A.; Kubota, T.; Ogata, Y.; Moossa, A. R.; Hoffman, R. M. *Anticancer Res.* **1997**, *17*, 1965–1971.
(79) Takeda, H.; Haisa, M.; Naomoto, Y.; Kawashima, R.; Satomoto, K.; Yamatucci, T.; Tanaka, N. *Jpn. J. Cancer Res.* **1999**, *90*, 677–684.
(80) Prinz, H. *J. Chem. Biol.* **2010**, *3*, 37–44.
(81) Wu, C. C.; Li, T. K.; Farh, L.; Lin, L. Y.; Lin, T. S.; Yu, Y. J.; Yen, T. J.; Chiang, C. W.; Chan, N. L. *Science* **2011**, *333*, 459–462.
(82) Dong, K. C.; Berger, J. M. *Nature* **2007**, *450*, 1201–1205.
(83) Monnot, M.; Mauffret, O.; Simon, V.; Lescot, E.; Psamme, B.; Saucier, J. M.; Charra, M.; Belehradek, J., Jr.; Fermandjian, S. *J. Biol. Chem.* **1991**, *266*, 1820–1829.
(84) Tewey, K. M.; Rowe, T. C.; Yang, L.; Halligan, B. D.; Liu, L. F. *Science* **1984**, *226*, 466–468.
(85) Capranico, G.; Zunino, F.; Kohn, K. W.; Pommier, Y. *Biochemistry* **1990**, *29*, 562–569.
(86) Mao, Y.; Okada, S.; Chang, L. S.; Muller, M. T. *Cancer Res.* **2000**, *60*, 4538–4543.
(87) Wang, P.; Leung, C. H.; Ma, D. L.; Lu, W.; Che, C. M. *Chem.—Asian J.* **2010**, *5*, 2271–2280.
(88) Pierson, V.; Pierre, A.; de Cointet, P.; Nguyen, C. H.; Bisagni, E.; Gros, P. *Biochem. Pharmacol.* **1989**, *38*, 1395–1406.
(89) Palchaudhuri, R.; Hergenrother, P. J. *Curr. Opin. Biotechnol.* **2007**, *18*, 497–503.
(90) Serratrice, M.; Cinelli, M. A.; Maiore, L.; Pilo, M.; Zucca, A.; Gabbiani, C.; Guerri, A.; Landini, I.; Nobili, S.; Mini, E.; Messori, L. *Inorg. Chem.* **2012**, *51*, 3161–3171.
(91) Statistical and graphing software: *KyPlot 5.0.2: Data Analysis and Visualization*, 5.0.2 ed.; Kyence Lab Inc.: Tokyo, Japan, 2011.
(92) Wojdyr, M. *J. Appl. Crystallogr.* **2010**, *43*, 1126–1128.
(93) *Oxford Diffraction*; Oxford Diffraction Ltd.: Yarnton, England, 2008.
(94) Sheldrick, G. M. *Acta Crystallogr.* **2008**, *A64*, 112–122.
(95) Dolomanov, O. V.; Bourhis, L. J.; Gildea, R. J.; Howard, J. A. K.; Puschmann, H. *J. Appl. Crystallogr.* **2009**, *42*, 339–341.
(96) Frisch, M. J. T.; Trucks, G. W.; Schlegel, H. B.; Scuseria, G. E.; Robb, M. A.; Cheeseman, J. R.; Scalmani, G.; Barone, V.; Mennucci, B.; Petersson, G. A.; Nakatsuji, H.; Caricato, M.; Li, X.; Hratchian, H. P.; Izmaylov, A. F.; Bloino, J.; Zheng, G.; Sonnenberg, J. L.; Hada, M.; Ehara, M.; Toyota, K.; Fukuda, R.; Hasegawa, J.; Ishida, M.; Nakajima, T.; Honda, Y.; Kitao, O.; Nakai, H.; Vreven, T.; Montgomery, J. A., Jr.; Peralta, J. E.; Ogliaro, F.; Bearpark, M.; Heyd, J. J.; Brothers, E.; Kudin, K. N.; Staroverov, V. N.; Kobayashi, R.; Normand, J.; Raghavachari, K.; Rendell, A.; Burant, J. C.; Iyengar, S. S.; Tomasi, J.; Cossi, M.; Rega, N.; Millam, J. M.; Klene, M.; Knox, J. E.; Cross, J. B.; Bakken, V.; Adamo, C.; Jaramillo, J.; Gomperts, R.; Stratmann, R. E.; Yazayev, O.; Austin, A. J.; Cammi, R.; Pomelli, C.; Ochterski, J. W.; Martin, R. L.; Morokuma, K.; Zakrzewski, V. G.; Voth, G. A.; Salvador, P.; Dannenberg, J. J.; Dapprich, S.; Daniels, A. D.; Farkas, Ö.; Foresman, J. B.; Ortiz, J. V.; Cioslowski, J.; Fox, D. J. *Gaussian 09W*; Gaussian Inc.: Wallingford, CT, 2009.
(97) Heyd, J.; Scuseria, G. J. *Chem. Phys.* **2004**, *121*, 1187–1192.
(98) Heyd, J.; Scuseria, G. E. *J. Chem. Phys.* **2004**, *120*, 7274.
(99) McLean, A. D.; Chandler, G. S. *J. Chem. Phys.* **1980**, *72*, 5639–5648.
(100) Raghavachari, K.; Binkley, J. S.; Seeger, R.; Pople, J. A. *J. Chem. Phys.* **1980**, *72*, 650–654.
(101) Hay, P. J.; Wadt, W. R. *J. Chem. Phys.* **1985**, *82*, 270–283.
(102) Wadt, W. R.; Hay, P. J. *J. Chem. Phys.* **1985**, *82*, 284–298.
(103) Ditchfield, R. *Mol. Phys.* **1974**, *27*, 789–807.
(104) Wolinski, K.; Hilton, J. F.; Pulay, P. *J. Am. Chem. Soc.* **1990**, *112*, 8251–8260.
(105) Barone, V.; Cossi, M. *J. Phys. Chem. A* **1998**, *102*, 1995–2001.
(106) Cossi, M.; Rega, N.; Scalmani, G.; Barone, V. *J. Comput. Chem.* **2003**, *24*, 669–681.
(107) Furche, F.; Ahlrichs, R. *J. Chem. Phys.* **2002**, *117*, 7433–7447.
(108) Scalmani, G.; Frisch, M. J.; Mennucci, B.; Tomasi, J.; Cammi, R.; Barone, V. *J. Chem. Phys.* **2006**, *124*, 094107:094101–094115.
(109) Reed, A. E.; Weinstock, R. B.; Weinhold, F. *J. Chem. Phys.* **1985**, *83*, 735–746.
(110) Tran, N. T.; Wang, T. H.; Lin, C. Y.; Tsai, Y. C.; Lai, C. H.; Tai, Y.; Yung, B. Y. *Bioconjug. Chem.* **2011**, *22*, 1394–1401.
(111) Schneider, C. A.; Rasband, W. S.; Eliceiri, K. W. *Nat. Methods* **2012**, *9*, 671–675.
(112) Straus, O. H.; Goldstein, A.; Plachte, F. L. *J. Gen. Physiol.* **1943**, *26*, 559–585.
(113) Shoichet, B. K. *J. Med. Chem.* **2006**, *49*, 7274–7277.